

AD-A216 043



DTIC
ELECTE
DEC 15 1989
S B D

OPTICAL AMPLIFICATION IN 45°-cut BaTiO₃

THESIS

Kenneth Scott Keppler
Captain, USAF

AFIT/GEO/ENG/89D-5

DEPARTMENT OF THE AIR FORCE
AIR UNIVERSITY

AIR FORCE INSTITUTE OF TECHNOLOGY

Wright-Patterson Air Force Base, Ohio

DISTRIBUTION STATEMENT A

Approved for public release;
Distribution Unlimited

89 12 14 019

AFIT/GEO/ENG/89D-5

OPTICAL AMPLIFICATION IN 45°-cut BaTiO₃

THESIS

Kenneth Scott Keppler
Captain, USAF

AFIT/GEO/ENG/89D-5

DTIC
ELECTE
DEC 15 1989
S B D

Approved for public release; distribution unlimited

AFIT/GEO/ENG/89D-5

OPTICAL AMPLIFICATION IN 45°-cut BaTiO₃

THESIS

Presented to the Faculty of the School of Engineering
of the Air Force Institute of Technology

Air University

In Partial Fulfillment of the
Requirements for the Degree of
Master of Science in Electrical Engineering

Kenneth Scott Keppler, B.S. Engineering
Captain, USAF

December, 1989

Approved for public release; distribution unlimited

Acknowledgments

I am indebted to three individuals for their contributions to this research effort. First, I would like to thank my advisor Major Steve Rogers for his help, guidance, and inspirational teaching ability. Without his interest and support of research in the electro-optics field, the expertise and equipment for this project would not have been available. Second, I would like to thank George Vogel for sharing the laboratory and most of the equipment used for experimentation. The extensive knowledge and experience he shared with me was as invaluable as his tremendous patience. Finally, I would like to thank Captain Jeff Wilson for developing much of the theory supporting this research and for all the valuable lessons learned that were passed on from his thesis work. All the work Jeff completed prior to my project, and the assistance he provided during this effort was tremendously appreciated.

I would also like to thank Lieutenant Colonel James P. Mills and Dr. Matthew Kabrisky for supporting my research as members of my thesis committee. I am grateful for their constructive comments on the draft version of the written report.

Special thanks is extended to all members of the DIME lab for sharing their experience, equipment, and engineering knowledge. I would especially like to thank Bob Cody, Dave Heatherington, and Pat White for providing and explaining various software packages used throughout my thesis effort. Technical and maintenance support provided by Dave Ridenour was also greatly appreciated.

Finally, I would like to thank my mother and father for inspiring me to set high educational goals and teaching me the self-discipline required to achieve them.

Kenneth Scott Keppler

on For	
RA&I	<input checked="" type="checkbox"/>
3	<input type="checkbox"/>
uced	<input type="checkbox"/>
ation	

By	
Distribution/	
Availability Codes	
Dist	Avail and/or Special
A-1	



Table of Contents

	Page
Acknowledgments	ii
Table of Contents	iii
List of Figures	v
Abstract	vii
I. Introduction	1
1.1 Background	1
1.2 Problem Statement	3
1.3 Sequence of Presentation	3
II. Summary of Current Knowledge	4
2.1 Introduction	4
2.2 Two-Wave Coupling	4
2.3 Photorefractive Scattering	14
2.4 Two-Wave Coupling in BaTiO ₃	16
III. Beam Fanning Testing	20
3.1 Introduction	20
3.2 Background Theory	20
3.3 Equipment and Procedure	21
3.4 Results	24

	Page
IV. Two-Wave Coupling Testing	31
4.1 Introduction	31
4.2 Background Theory	31
4.3 Equipment and Procedure	33
4.4 Results	37
V. Image Amplification Testing	58
5.1 Introduction	58
5.2 Background Theory	58
5.3 Equipment and Procedure	59
5.4 Results	61
VI. Conclusions and Recommendations	67
6.1 Conclusions	67
6.2 Recommendations	68
Bibliography	70
Vita	72

List of Figures

Figure	Page
1. Two-Wave Coupling Interference Fringes	6
2. Photorefractive Effect with Shifted Index Grating	7
3. Diffraction of Two-Wave Coupling Input Beams	9
4. Output Beam Interference for an Unshifted Index Grating	10
5. Output Beam Interference for a Shifted Index Grating	11
6. Two-Wave Coupling Gain Parameters	12
7. 45°-cut BaTiO ₃ Crystal	17
8. Two-Wave Coupling Geometry	18
9. Beam Fanning Test Set-up	22
10. Dimensions of crystal #115-F	23
11. Transmitted Intensity versus Time for $\theta = 0$	25
12. Transmitted Intensity versus Time for Various Entrance Angles	27
13. Transmitted Intensity versus Time for Various Input Intensities	28
14. Beam Fanning Input Beam Positions	29
15. Transmitted Intensity versus Time for Various Input Positions	30
16. Two-Wave Coupling Input Geometry	32
17. Two-Wave Coupling Experimental Set-up	34
18. Pump and Signal Beam Positions Inside the Crystal	36
19. Output Power versus Time, $P_p(0)=10$ mW, $P_s(0)=1.0$ mW	39
20. Pump Beam Output Power versus Time	39
21. Transmitted Pump Power with and without an Input Signal Beam	40
22. Output Power versus Time, $P_p(0)=10$ mW, $P_s(0)=0.10$ mW	41
23. Output Power versus Time, $P_p(0)=10$ mW, $P_s(0)=0.01$ mW	41
24. Signal Beam Output Power versus Time for a 10 mW Pump	43

Figure	Page
25. Signal Beam Output Power versus Time for a 1.0 mW Pump	44
26. Signal Beam Output Power versus Time for a 0.1 mW Pump	45
27. Output for Extraordinarily-polarized Input Beams	47
28. Output for 45° CW Polarization Rotation	47
29. Positions of Power Measurements used to calculate Γ	49
30. Log G_{pk} versus Log $P_s(0)$ for Crystal #115-F	51
31. Log G_{pk} versus Log $P_s(0)$ for Crystal #133-E	52
32. Log G_{ss} versus Log $P_s(0)$ for Crystal #115-F	53
33. Peak Gain versus β , $P_p(0)=1.0$ mW, $P_s(0)=0.1$ mW	54
34. Output Power versus Time, $P_p(0)=1.0$ mW, $P_s(0)=0.1$ mW	56
35. Signal Output Power versus Time for a Pre-fanned Pump Beam	56
36. Optical Associative Memory in a Confocal Resonator	59
37. Experimental Set-up for Fourier Transform Amplification	60
38. Experimental Set-up for Image Amplification	62
39. Overlapping Amplified Resolution Chart Image	63
40. Double Internal Reflection of the Signal Beam	65

Abstract

Two-wave coupling in BaTiO_3 has been widely investigated because of the high gains predicted theoretically. Unfortunately, the high gain also amplifies pump and signal light scattered from imperfections inside the crystal. In this report, optical scattering (or beam fanning) and its effects on two-wave coupling gain and image amplification are investigated for 45° -cut BaTiO_3 crystals.

Experimental set-ups for beam fanning, two-wave coupling, and image amplification were designed to investigate signal and image outputs versus time. During beam fanning testing, records of transmitted intensity of a single input beam versus time were obtained for various entrance angles, and input intensities. Pump and signal output powers versus time were recorded for two-wave coupling tests. Input pump beam powers of 10, 1.0, and 0.1 mW were tested at a wavelength of 514.5 nm. Signal input beam powers ranging from 1.0 to .001 mW were used. In image amplification tests, the Fourier transform and a minified image of a resolution chart were amplified via two-wave coupling.

Data from beam fanning and two-wave coupling tests implied that the beam fanning of the pump beam has negligible effect on the two-wave coupling gain of the output signal. Following rise to a peak value, the output signal beam power decreased due to fanning of the amplified signal beam for input pump powers of 10 and 1.0 mW. Little or no drop-off was observed for the 0.1 mW input pump power. A linear relationship between the logarithm of the gain (peak and steady-state) and the logarithm of the input signal power was discovered over the entire range of the input pump and signal powers tested. Amplification of the resolution chart's Fourier transform resulted in an edge enhanced image. Secondary images were observed for both image amplification set-ups.

OPTICAL AMPLIFICATION IN 45°-cut BaTiO₃

I. Introduction

1.1 Background

Electronic computers have tremendous difficulty solving pattern recognition problems that humans can solve with ease. Optical computing architectures are being investigated as alternatives to electronic computing architectures for pattern recognition systems. One potential architecture for optical computers is by mimicking biological computers such as artificial neural networks.

Artificial neural network models, or neural nets, have been used to mathematically model the simple characteristics of the way the brain processes information. A neural net simulates the interactions that occur between a large number of neurons or brain cells. Conventional (von Neumann) computers process information sequentially, while a neural net can process many inputs simultaneously (i.e. - in parallel). Although a detailed explanation of neural networks is beyond the scope of this discussion, it is important to understand that neural nets provide an architecture that allows more efficient processing of information than conventional computers for certain types of problems. Lippmann, in a paper reviewing neural nets, states "... human-like performance in the areas of speech and image recognition will require enormous amounts of processing. Neural nets provide one technique for obtaining the required processing capability using large numbers of simple processing elements operating in parallel (13:5)".

Interestingly, optical technology allows interconnection of a large number of processing elements. Unlike electrical paths in semiconductor chips, light rays can

come close to one another and even cross without affecting each other. Thus, optical hardware appears well suited for fabricating neural net systems.

A number of neural network systems have recently been developed using optical hardware. One type of system related to the task of pattern recognition is the holographic or optical associative memory. An associative (or content-addressable) memory is a system that can reproduce a stored signal given a distorted or incomplete version of the signal. A Hopfield net is a neural net that can be designed as an associative memory (13:6). Optical associative memories based on the theory of Hopfield nets have been demonstrated (6) (18) (3) (22). Key elements of each system include memory and thresholding devices, and the feedback loop. The images to be recalled are stored (in memory) as holograms on a glass plate or a non-linear optic crystal. Thresholding devices allow the system to decide which stored image most resembles the input image. Non-linear optical materials such as barium titanate (BaTiO_3) and gallium arsenide (GaAs) have been used for thresholding correlations between the input and stored images (22) (1). Ring and phase conjugate resonators are two types of feedback loops that have been used.

During his thesis research, Wilson investigated the feasibility of a confocal resonator architecture for an optical associative memory (25). Final system operation was not demonstrated; however, Wilson developed the general theory supporting the architecture, built the resonator structure, and investigated image amplification using BaTiO_3 . The resonator (called a Confocal Fabry-Perot Resonator) consists of two meniscus concave shaped mirrors with reflective coatings on the back side. The mirrors are mounted to a rigid structure and their positions are electronically controlled. The focal points of the two mirrors are coincident (thus the confocal name). Characterization of the image amplification capabilities of BaTiO_3 proved to be a tremendously difficult task. All previously documented results for BaTiO_3 were for a crystal cut in which the \hat{c} or optic axis was parallel to four crystal faces and perpendicular to the other two (z-cut crystal). The higher gains achievable with

45°-cut BaTiO₃ crystals amplify light scattered by crystal imperfections resulting in optical scattering (or beam fanning).

1.2 Problem Statement

This thesis is a direct follow-on of the research investigating Optical Information Processing in a Confocal Fabry-Perot Resonator completed by Captain Jeffery A. Wilson in December 1988. The purpose of this research is to characterize the performance of 45°-cut BaTiO₃ crystals to be used for optical image amplification in an optical associative memory using a Confocal Fabry-Perot resonator architecture. Since beam fanning is so pronounced in the 45°-cut crystals, input parameters and/or conditions that may reduce fanning must be investigated. Effects of beam fanning on the gain and temporal behavior of two-wave coupling need to be determined. Image amplification via two-wave coupling must then be evaluated for use in the resonator architecture.

1.3 Sequence of Presentation

Experimental tests were performed to determine methods for reducing beam fanning effects on two-wave coupling image amplification. Investigation of optical amplification capabilities of the two BaTiO₃ crystals available was accomplished in three main parts. First, beam fanning of a single input beam was investigated as a function of entrance angle, beam diameter, and intensity. Then, two-wave coupling amplification of a 1.5 mm diameter input signal beam was determined as a function of pump power, signal beam power, and input angle relative to the crystal face. Finally, optical amplification of a resolution chart was investigated via two-wave coupling of an image and a Fourier transform of the chart. In the next chapter, a summary of the current knowledge on two-wave coupling, beam fanning, and two-wave coupling in BaTiO₃ crystals is presented.

II. Summary of Current Knowledge

2.1 Introduction

When an image enters a loop in an optical system, the intensity is reduced each time the image is transmitted through or reflected from an optical element in the loop. Without amplification inside the loop, the input image will eventually die out. Two-wave coupling in electro-optic crystals is a method of amplifying an optical signal (or image). Optical amplification via two-wave coupling, inside a confocal resonator, will allow the iterative image processing required for operation of an optical neural network. This chapter is a discussion of two-wave coupling, and beam fanning theory related to BaTiO_3 . Background principles of two-wave coupling will be discussed first, then optical scattering (or beam fanning). Finally, results of two-wave coupling with BaTiO_3 crystals will be discussed.

2.2 Two-Wave Coupling

The interference pattern of two light beams inside an electro-optic crystal results in a proportional change in the index of refraction inside the crystal. This stored index pattern or index grating is formed throughout the entire volume of the crystal. Thus, the grating pattern is most commonly referred to as a volume (or thick-phase) hologram. When the location of the grating is spatially shifted relative to the original interference pattern, energy from one of the incident beams is transferred to the other beam. This energy transfer is known as beam coupling or two-wave coupling.

Since Kogelnik's article on coupled wave theory in 1969 (11), many papers and articles discussing two-wave coupling have been written. One of the most recent and comprehensive works is a paper by Günter (9). The following discussion is based on Günter's paper, and a number of articles on two-wave coupling (21) (4) (2).

In order to understand how two-wave coupling occurs, one must first understand how volume holograms are created. The process responsible for the light-induced change of index of refraction is called the photorefractive effect. Günter states, "...with a detailed knowledge of the photorefractive recording mechanisms it is possible to optimize the grating phase shift with a suitable choice of physical parameters ...and to control the gain in energy transfer experiments with these parameters (9:204)".

The first step in creating a volume hologram is to create an interference pattern in the crystal using two mutually coherent light beams. Assume, for simplicity, that the two input (or recording) beams are plane waves incident on the crystal as shown in Figure 1a. If both beams are propagating in the xz plane, the irradiance pattern resulting from the interference of the two beams will be a set of fringes with a sinusoidally varying intensity as shown in Figure 1b. This is shown mathematically by Staebler and Amodei (21:1042-1043). Note that Figure 1b is the intensity variation for any plane parallel to the xz plane, inside the crystal.

The photorefractive effect creates light induced refractive index changes by creating electric fields inside the crystal as shown in Figure 2. The process begins when light of the proper wavelength excites charge carriers (either electrons or holes) from impurity centers in the crystal. The free charges migrate until they are retrapped at other locations, and leave behind opposite charges of ionized trap centers. The migration/retrap process is repeated until the photo-excited charges drift out of the illuminated region and are finally trapped in darker regions. The result is a space-charge density distribution, ρ_{sc} , modulated by the irradiance of the interference pattern as shown in Figure 2b. This space-charge density distribution creates an electric space-charge field, E_{sc} (see Figure 2c). Finally, the E_{sc} modulates the index of refraction via the linear electro-optic effect. Notice that the change in index of refraction is 180 degrees out of phase with E_{sc} (Figure 2d). Depending on the type of crystal and the illumination conditions, ρ_{sc} may or may not be shifted

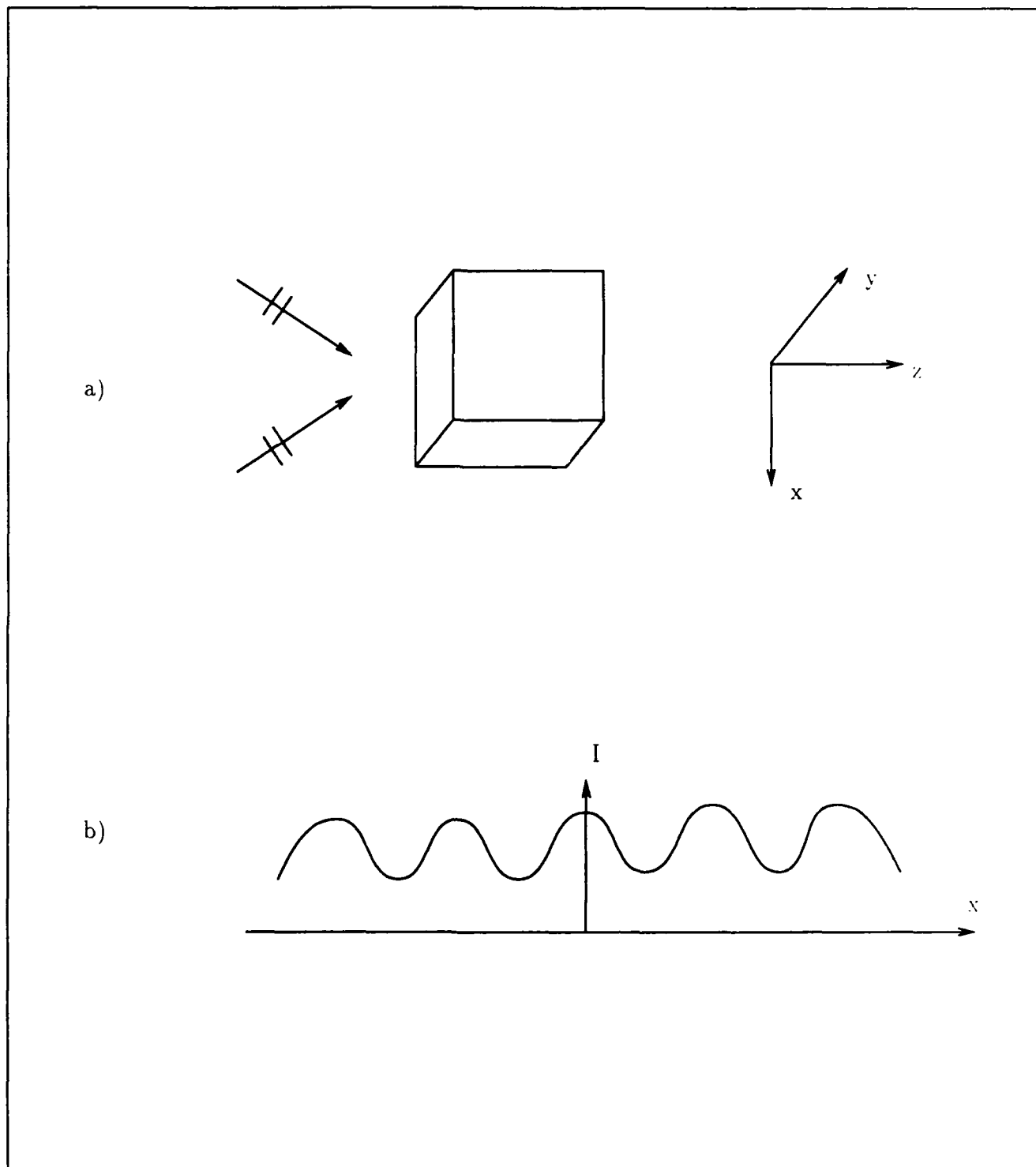


Figure 1. Two-Wave Coupling Interference Fringes

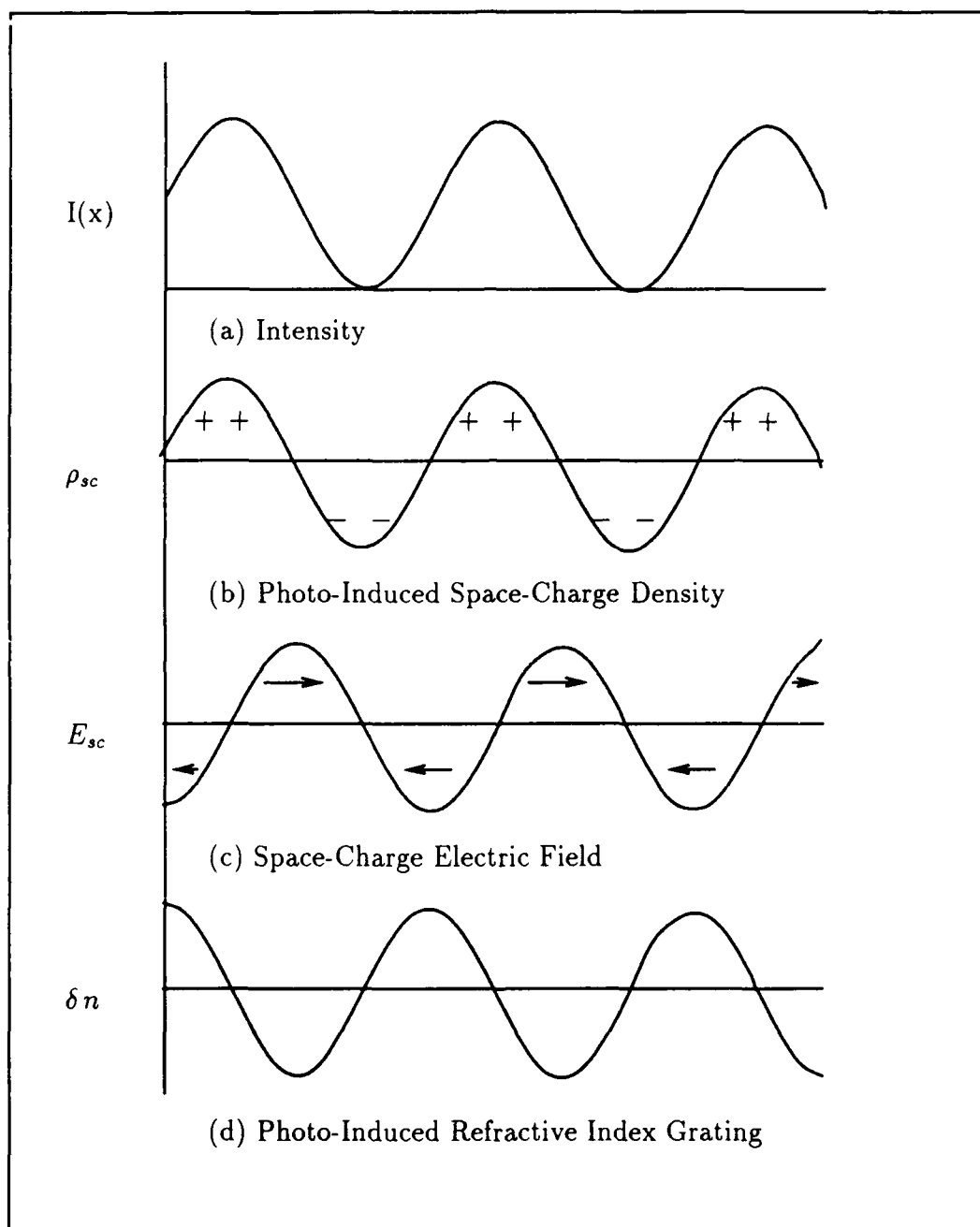


Figure 2. Photorefractive Effect with Shifted Index Grating

with respect to E_{sc} .

The shift of the space-charge field with respect to the charge density distribution depends on the type of charge transfer process, the illumination geometry, and the type of crystal. Photorefractive materials have three main charge transport processes: diffusion, volume photovoltaic effect, and photoconductivity (drift in an applied electric field) (9:219). Diffusion is the dominant transport process for a BaTiO₃ crystal with no externally applied field. When diffusion is the dominant charge carrier for a crystal, the electric space-charge field is shifted by 90 degrees with respect to the space-charge density distribution (reference Figure 2).

The final step in the hologram formation process is the change in the index of refraction of the material. The internal space-charge field modulates the crystal's index of refraction via the linear electro-optic effect. When the two input beams are ordinarily polarized (i.e. - electric field vectors are parallel to the z-axis in Figure 1), the change in index of refraction along the x direction for BaTiO₃ is given by (4:47)

$$\delta n_{ord} = -\frac{1}{2} n_o^3 r_{13} E_{sc} \quad (1)$$

where n_o is the ordinary index of refraction, r_{13} is the appropriate electro-optic (or Pockels) coefficient for BaTiO₃, and E_{sc} is the value of the electric space-charge field. From Equation 1 it is apparent that the change in index of refraction is proportional to and 180 degrees out of phase with the electric space-charge field. Thus, the index grating is shifted with respect to the original intensity distribution.

In order to understand how energy can be transferred from one beam to the other, the three dimensional index grating pattern formed in the crystal can be considered analogous to a set of diffraction planes (planes of constant refractive index) that are parallel to the sides of the crystal as shown in Figure 3. Input beams traveling in the directions shown in Figure 3 create the index grating. As the grating builds, the diffraction planes transmit and diffract (via Bragg diffraction) portions

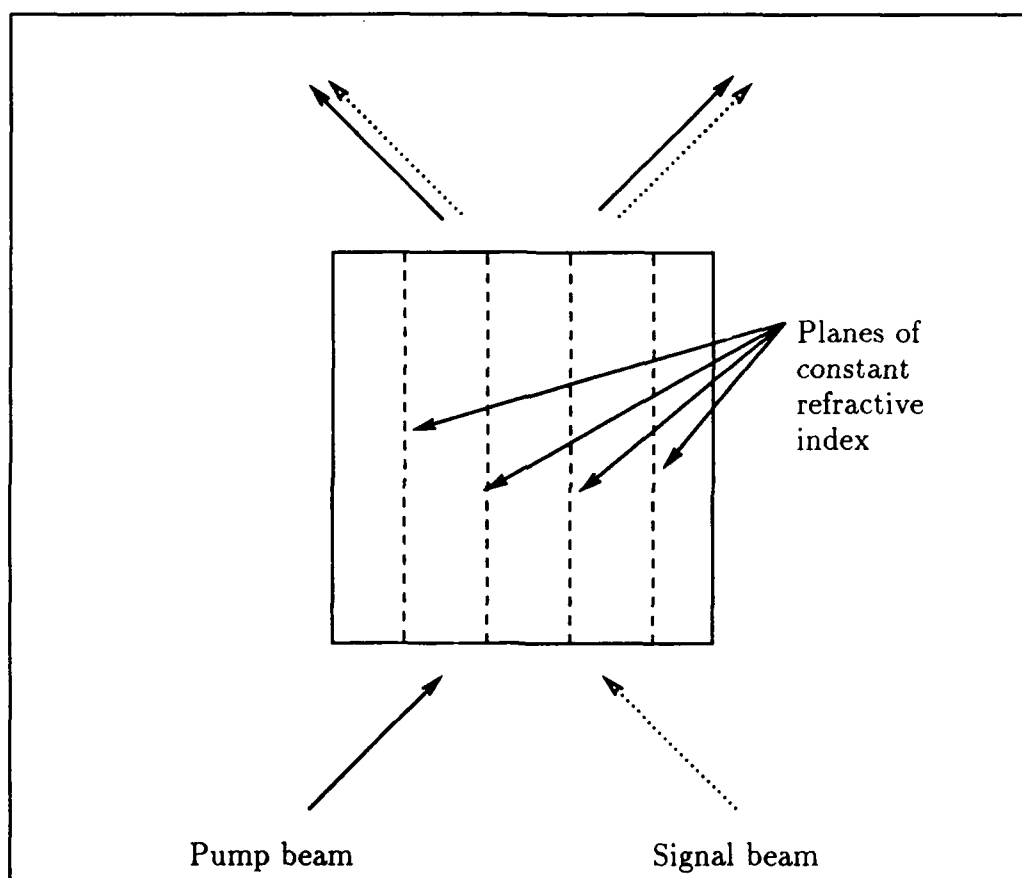


Figure 3. Diffraction of Two-Wave Coupling Input Beams

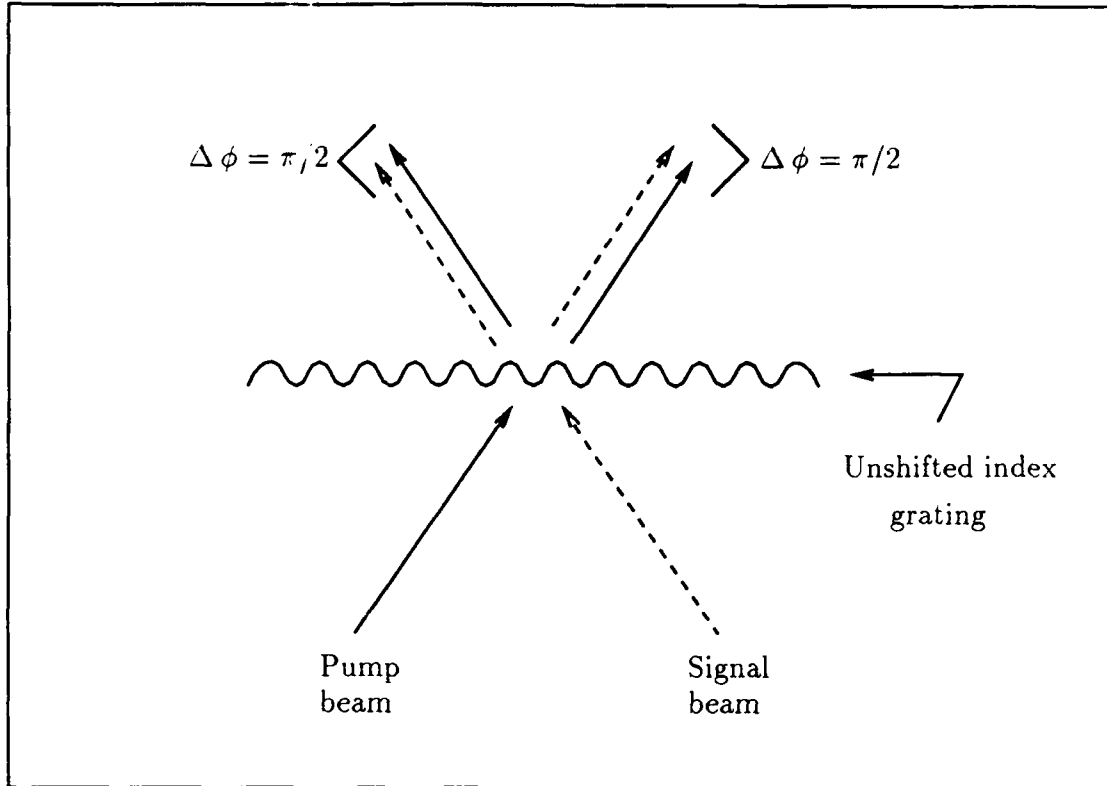


Figure 4. Output Beam Interference for an Unshifted Index Grating

of each input beam. Notice that the diffracted portion of each beam is in the same direction as the transmitted portion of the other beam. The diffraction plane analogy explains why only one diffracted order is transmitted for each input beam. A thin diffraction grating is not a proper analogy in this case, as it would produce positive and negative first order diffraction pairs for each input beam.

The electric space-charge field must be shifted with respect to the space-charge density distribution for energy transfer between the two input beams to occur. If there is no shift, the phase difference ($\Delta\phi$) between the first order Bragg diffracted signal beam and the transmitted reference (pump) beam traveling in the same direction is $\pi/2$, resulting in destructive interference between the two beams (see Figure 4). Günter states that, "A maximum energy transfer is therefore obtained, if

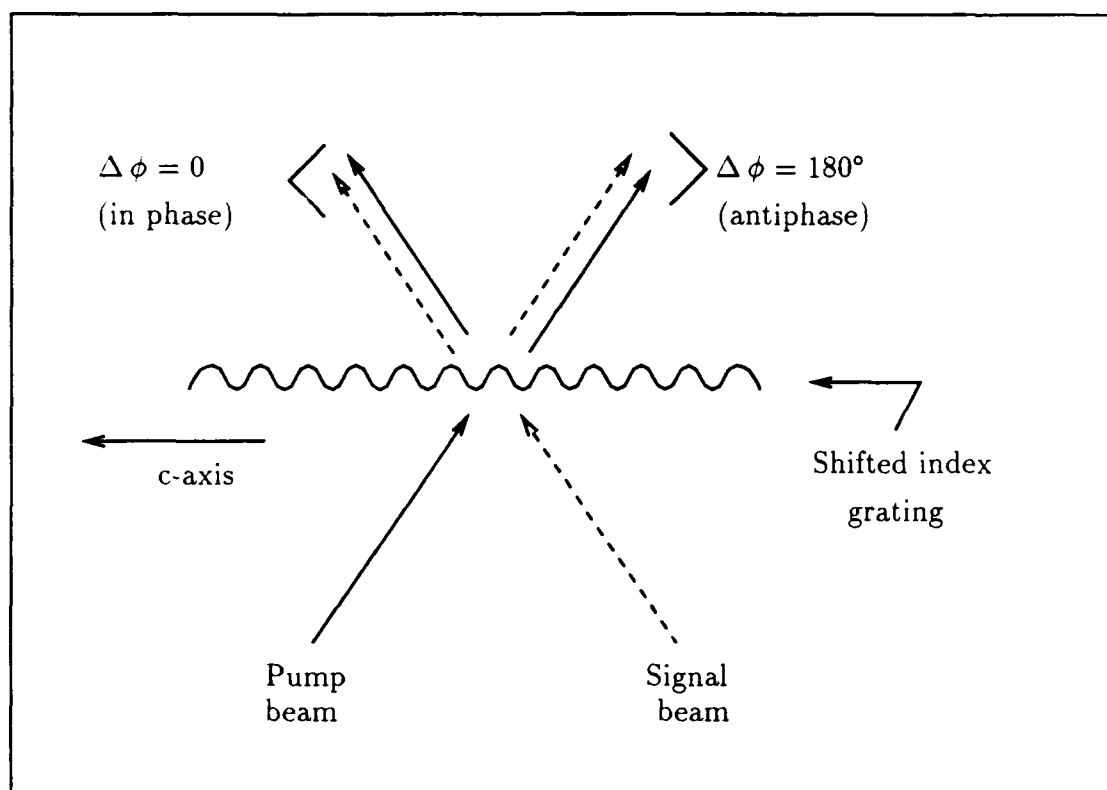


Figure 5. Output Beam Interference for a Shifted Index Grating

there is an additional phase shift of $\pi/2$ between the undiffracted signal beam and the diffracted reference beam. This is the case for a stationary grating phase shift of $\pi/2$ with respect to the intensity distribution (9:244).” As shown in Figure 5, a grating shifted by $\pi/2$ with respect to the original interference pattern allows two diffracted orders traveling in the same direction to be in phase and add constructively (acceptor beam). The other pair of diffracted orders are in antiphase and add destructively (donor beam). The energy transfer or coupling of the beams is a direct result of the change in relative phase of the two diffracted order pairs caused by the shifted index grating. Günter does not clearly state the cause of the $\pi/2$ phase shift between diffracted orders in the same direction for an unshifted grating. The shift appears to be an empirical result that satisfies the condition of energy conservation for the input and output beams.

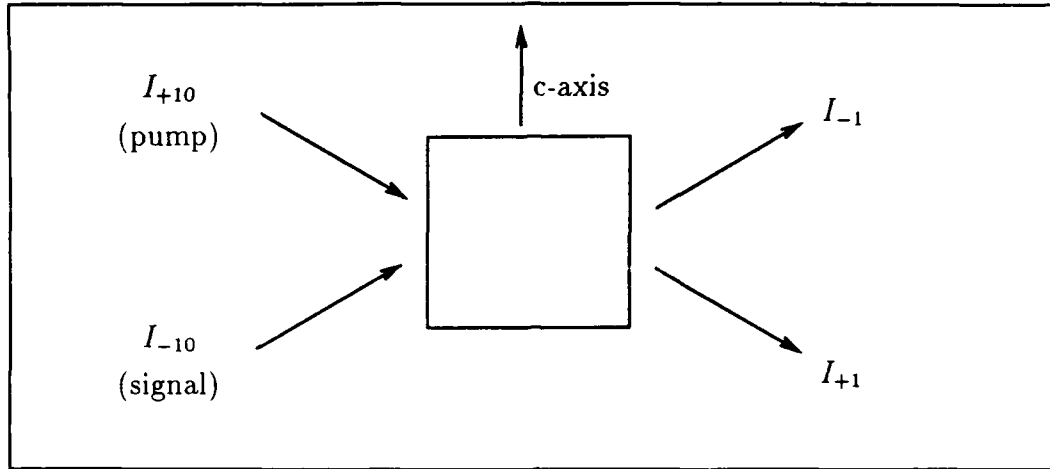


Figure 6. Two-Wave Coupling Gain Parameters

According to Günter, "Volume hologram formation by the photorefractive effect and energy transfer between interacting beams must be simultaneously described by a 'dynamic' theory, which takes into account any possible changes of the fringe-pattern contrast along the crystal length due to the intensity redistribution between the two writing beams (9:246)." Using the coupled wave theory of Kogelnik (11) Günter derives an expression for the exponential gain coefficient (9:246-249)

$$\Gamma = \frac{1}{d} \ln \left(\frac{I_{-1}}{I_{-10}} \cdot \frac{I_{+10}}{I_{+1}} \right) \quad (2)$$

where d is the interaction distance of the two beams inside the crystal, $I_{+10,-10}$ are the incident beam intensities, and $I_{+1,-1}$ are the steady-state intensities of the diffracted beams (see Figure 6). Marrakchi and Huignard report an identical expression for Γ based on Kukhtarev and Vinetskii's theory deriving the two beam intensities from the complete set of charge transport and coupled wave equations (16:132). The exponential gain coefficient characterizes the efficiency of energy transfer between the two input beams.

When discussing energy transfer, both Günter (9:253) and Marrakchi (16:133)

define an "effective gain", γ_o , as the ratio of the intensity of I_{-1} in the presence of the pump beam I_{+10} to I_{-1} without the pump beam. Therefore, γ_o can be expressed in terms of Γ as,

$$\gamma_o = \frac{I_{-1} \text{ with pump beam}}{I_{-1} \text{ without pump beam}} = \frac{(1+r)e^{\Gamma d}}{1+re^{\Gamma d}} \quad (3)$$

where $r = I_{-10}/I_{+10}$ is the ratio of the input signal beam to the input pump beam. Thus, the gain in output signal intensity can be predicted for a given input pump to signal ratio if Γ and the interaction length of the two beams in the photorefractive media are known.

Note that two-wave coupling is not an instantaneous process like other non-linear optical processes (i.e. - sum frequency mixing). The time required to build up the grating depends on the charge transfer process, the illumination intensities, and the illumination geometry. Once formed, however, the hologram will remain until erased by light (coherent or incoherent) of sufficient intensity.

In summary, two-wave coupling is the result of an index grating that is shifted with respect to the interference pattern created by two input light beams. The interference pattern allows charge migrations between regions of varying illumination in the crystal. The resulting charge distribution is proportional to the intensity of the interference pattern. If diffusion is the dominant charge transfer process, an electric space-charge field that is phase shifted with respect to the charge distribution will form. This field modulates the index of refraction inside the crystal via the linear electro-optic effect. The grating shift with respect to the original intensity pattern allows diffraction of energy from one beam to the other. Using coupled wave theory, characteristic two-wave coupling parameters can be derived. These parameters will be used in following chapters. Due to observed effects on two-wave coupling gain in BaTiO₃, photorefractive scattering is discussed next.

2.3 Photorefractive Scattering

A single laser beam passing through a photorefractive crystal will initially have a transmitted irradiance profile similar to the irradiance profile incident on the crystal. After a few seconds, however, the transmitted irradiance profile begins to spread. Energy from the beam appears to scatter or fan out mainly to one side of the beam. Numerous articles have recently been written on this scattering effect, and many terms have been used to describe it including: light-induced scattering (19), stimulated photorefractive scattering (24), anisotropic scattering (23), asymmetric scattering (17), asymmetric self-defocusing (4), photorefractive fanout (7), and beam fanning (4). In this section, causes of beam fanning and parameters affecting it will be discussed.

Although beam fanning has been widely investigated, the process responsible for producing it is, like two-wave coupling, not completely understood. In fact, beam fanning is in part described by two-wave coupling. The light beam incident upon the crystal is scattered by imperfections or impurities in the crystal. The scattered light is still coherent with the transmitted portions of the beam. Thus, two-wave coupling can occur between each scattered beam and the original (pump) beam. Random gratings written by the incident beam and the light beams scattered from the crystal inhomogeneities result in beam fanning (19:223). Valley states that some of the amplified waves "... may actually be Fresnel reflections of the pump beam from the crystal-external-medium interface or from crystal striations (24:14)."

Mathematical models describing the simultaneous interactions between beam fanning and two-wave coupling do not exist; however, many parameters have been observed that affect the beam fanning irradiance pattern. Rupp and Dress proposed the following expression for the ratio of the transmitted intensity of the pump (incident) beam as a function of time, $I_p(t)$, to the initial pump beam intensity, $I_p(0)$

(19:224),

$$\frac{I_p(t)}{I_p(0)} = \frac{1 + m_o}{1 + m_o \exp(\Gamma_{eff} d)} \quad (4)$$

where, $m_o = I_s(t = 0)/I_p(t = 0)$ is the initial scattering ratio of the scattered wave to the pump, $\Gamma_{eff} = \Gamma[1 - \exp(-t/\tau)]$, an effective coupling constant that must be determined experimentally, and d is the interaction distance between the two beams. Γ , in the expression for Γ_{eff} , is the two-wave gain coefficient defined in Equation 2. Equation 4 is a version of Kukhtarev's solution to the coupled wave equation, slightly modified to be appropriate for scattering.

Both crystal and input beam parameters affect the amount of observed beam fanning. Crystal parameters include crystal type, orientation relative to input beam, and thickness of the crystal. Rupp and Dress present experimental data for lithium niobate showing an exponential reduction in the ratio of the steady-state value of the pump output, $I_p(\infty)$, to the initial pump output, $I_p(0)$. Input beam parameters affecting the beam fanning output include intensity, polarization, diameter, and wavelength. As will be shown experimentally in the next chapter, increasing the intensity of the beam generally increases the fanning intensity and the rate at which fanning occurs. Rotating the polarization of the input beam changes the value of the effective electro-optic coefficient. This in turn, changes the amount of two-wave coupling gain. In BaTiO₃, light polarized extraordinarily (i.e. - in the plane of the direction of propagation and the crystal \hat{c} -axis) provides the maximum two-wave coupling gain, and therefore, maximum beam fanning. Moore and Walters report an increase in beam fanning for BaTiO₃ with an increase in beam size for a constant beam power (i.e. - the larger the beam size, the larger the fanning with constant input power). In addition, they found only a one percent change in the mean ratio of incident intensity to fanned intensity across a wavelength range of 458 to 514.5 nm (17:1806- 1809). In contrast, Rupp and Dress found increasing scattering with decreasing wavelength for a range of 477 to 676 nm (19:227).

In summary, beam fanning is a photorefractive process in which light scattered

by crystal inhomogeneities is amplified via two-wave coupling. In certain applications of photorefractive crystals, such as self-pumped phase conjugation (14), strong beam fanning is desirable. However, image amplification via two-wave coupling may be adversely affected by beam fanning, as discussed in the next section.

2.4 Two-Wave Coupling in BaTiO_3

Two-wave coupling gain for any photorefractive crystal depends on the sensitivity of the crystal to the input light beams. One measure of the sensitivity is the value of the electro-optic coefficients for a given crystal. In BaTiO_3 the value of the r_{42} and r_{31} coefficients is 1640×10^{-12} m/V (26:232). This is almost two orders of magnitude larger than coefficients for most other photorefractive materials. In comparison, the highest coefficient for lithium niobate is $r_{33} = 30.5 \times 10^{-12}$ m/V (26:232). Due to the large electro-optic coefficient, BaTiO_3 appears to be a good candidate for image amplification via two-wave coupling.

Although BaTiO_3 has high electro-optic coefficients, the manufacturing process is difficult and can strongly affect the photorefractive characteristics of the crystal. Two different crystal growth processes have been reported. Günter states that the melt grown crystals show better qualities than the flux grown crystals (9:239). All BaTiO_3 crystals used in this project are melt grown crystals prepared by Sanders Associates (20). During the crystal growth process, adjacent unit cells may have polarization vectors that do not point in the same direction. Cells with perpendicular and parallel (but opposite) polarization vectors form 90 degree and 180 degree ferroelectric domain walls respectively. A process known as 'poling' is performed mechanically and electrically to remove 90 and 180 degree domains. The result is a single domain crystal (i.e. - a crystal with the polarization vectors of all unit cells pointed in one direction). Another consideration regarding the manufacture of BaTiO_3 crystals is the type of cut. The two options currently available are the z-cut and the 45°-cut. The z-cut crystal is cut so that the \hat{c} -axis of the crystal is parallel to

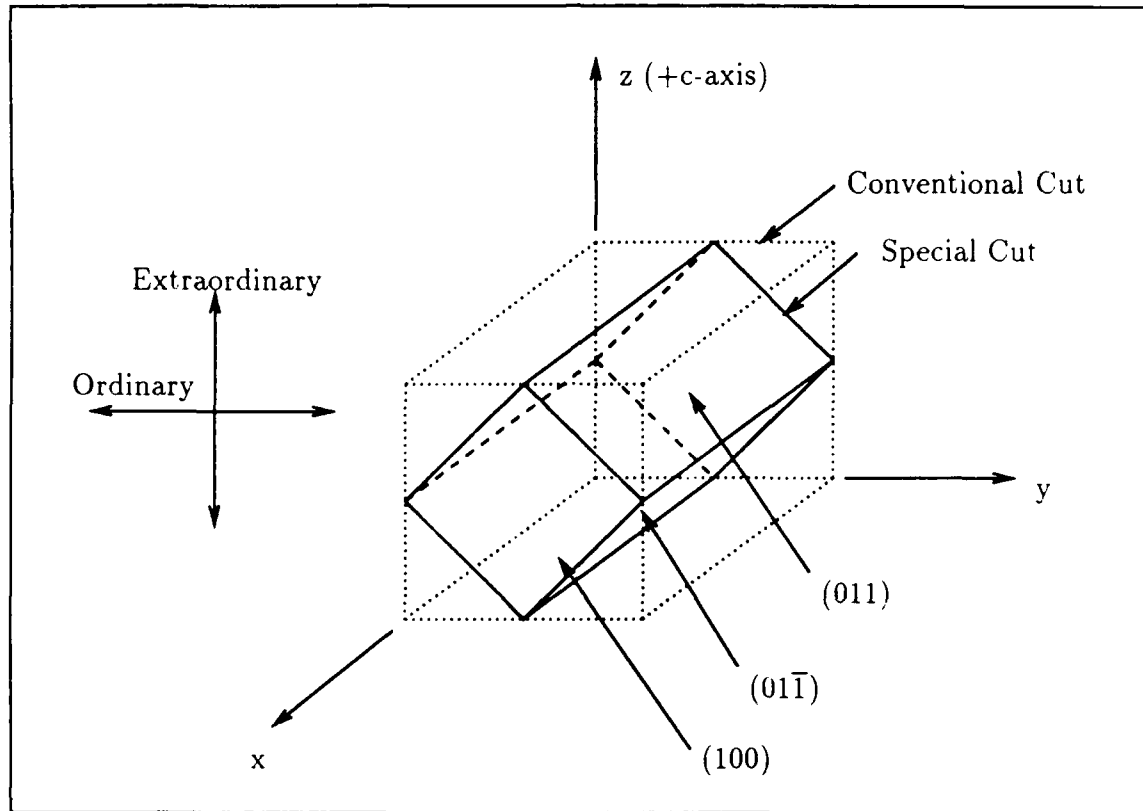


Figure 7. 45°-cut BaTiO₃ Crystal

four faces of the crystal and perpendicular to the remaining two faces. The 45°-cut crystal has a \hat{c} -axis at 45 °to two adjacent faces as shown in Figure 7 (2:234) (25:7).

The photorefractive properties of BaTiO₃ have been extensively investigated in the past ten years. However, the vast majority of theory describing volume holography and two-wave coupling is based on experiments performed using lithium niobate. Since BaTiO₃ is a relatively new type of crystal, its photorefractive behavior is still not completely understood. For example, the species (i.e. - charge carrier) responsible for the photorefractive effect in BaTiO₃ is still unknown. In addition, the charge migration process is described by two different models (12) (4). Marciniak derives the expressions for both models in detail. He concludes that for both models, "... the key factor in two-beam coupling is the phase shift between the electro-static field

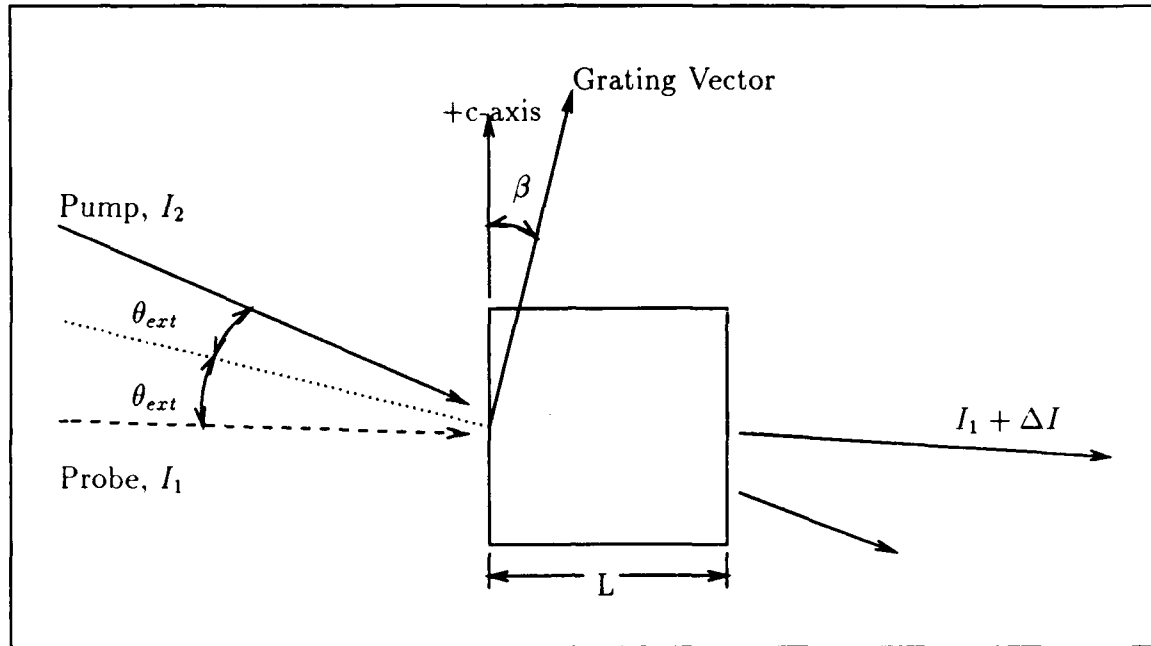


Figure 8. Two-Wave Coupling Geometry

and the incident interference fringes (15)."

Fainman *et al.* developed theoretical expressions for the two-wave coupling gain coefficient, Γ , and verified the model with experimental results obtained using a z-cut BaTiO₃ crystal. The model predicts Γ values as a function of the angle, 2θ , between the propagation directions of the two input beams (inside the crystal), and the angle, β , of the index grating vector with the crystal c-axis. The grating vector is the direction perpendicular to the bisector of the input beam propagation directions inside the crystal (see Figure 8 (25:36)). Note that the angle 2θ (inside the crystal) is related to the angle $2\theta_{ext}$ (outside the crystal) by Snell's law. A maximum Γ of 3.6 mm^{-1} was predicted for $\theta = 2^\circ$ and $\beta = 45^\circ$. These conditions could not be achieved with a z-cut crystal due to the high index of refraction, and consequently, the large bending of the input light beams. Therefore, they recommended a 45° -cut crystal be manufactured to allow access to the higher Γ with near normal incident beams.

Wilson obtained Γ values corresponding to those documented by Fainman *et al.* for a z-cut BaTiO₃ crystal (25:50). However, experimentation with two 45°-cut crystals yielded unexpected results. The large Γ obtainable with the 45°-cut crystals apparently resulted in measurable beam fanning of both the pump and the signal beams. The loss in pump beam power resulted in Γ values that were lower than the z-cut crystal Γ values. In addition, Wilson reported that the signal beam intensity increased to a peak value, and then rapidly decreased back to or below the original intensity (i.e. - steady-state gain did not occur). Wilson recommended that a mathematical model be developed to determine the effect of beam fanning on two-wave coupling gain.

An as yet unpublished article by Ford *et al.* (8), reported a maximum Γ value of 2.6 mm⁻¹ using a thinner (2.5 mm) 45°-cut crystal. The 2.5 mm crystal allowed more gain per unit length with less beam fanning, and produced higher gains than were achieved using a z-cut crystal.

In summary, two-wave coupling gains for z-cut BaTiO₃ crystals are predictable through theoretical methods. Due to the effects of beam fanning, a mathematical model for predicting two-wave coupling gains in 45°-cut BaTiO₃ has not yet been determined. In the next chapter, beam fanning tests of the 45°-cut BaTiO₃ crystals are investigated.

III. Beam Fanning Testing

3.1 Introduction

Wilson's observation of a drop-off in two-wave coupling output signal power, following an increase to a peak value, was attributed to beam fanning. Prior to testing, two problems caused by beam fanning appeared to reduce the effectiveness of optical amplification in 45°-cut BaTiO₃ crystals. The first problem was the depletion of the pump beam power. This depletion seemed to reduce the pump gain available for amplification of the input signal or image. The second problem was amplification of scattered light (from the pump beam) that is transmitted in the direction of the amplified image. The amplified scattered light is a type of optical noise that reduces the signal to noise ratio of the amplified output image. Image distortion will increase as the amount of amplified scattered light increases. This chapter investigates the depletion of the pump beam due to amplification of scattered light. Background theory related to the pump beam transmission versus time will be presented first. Then, the test procedure and equipment used will be described. A discussion of the test results concludes the chapter. The optical noise problem will be discussed as part of the following chapter.

3.2 Background Theory

Rupp and Dress investigated beam fanning properties of LiNbO₃ and z-cut BaTiO₃ crystals (19:223-229). As previously discussed in Section 2.3, they proposed the following expression for output intensity as a function of time for a single beam incident upon a photorefractive crystal,

$$\frac{I_p(t)}{I_p(0)} = \frac{1 + m_o}{1 + m_o \exp\{\Gamma[1 - \exp(-t/\tau)]\}} \quad (5)$$

where $m_o = I_{sc}(0)/I_p(0)$, Γ is the crystal gain coefficient, and τ is the dielectric relaxation time. Note that m_o is the ratio of the scattered wave intensity, $I_{sc}(0)$, in one direction to the pump (or input) beam intensity. The scattered wave intensity is denoted as $I_{sc}(0)$ in this chapter (rather than as $I_s(0)$ as in the Rupp and Dress article) to avoid confusion with the input signal beam intensity $I_s(0)$ used in the next chapter. Due to the difficulty in measuring $I_{sc}(0)$, m_o is not determined by direct experimental measurement. Although Equation 5 was proposed as a "crude approximation", the model when fitted to their experimental data was "surprisingly successful"(19:227). Based on the success of Rupp and Dress's model, beam fanning test data collected during this thesis effort was used to estimate the parameters m_o , Γ , and τ for each test condition. The curve fitting details and discussion of the results will be presented in an AFIT dissertation to be published in June 1990 by George Vogel.

The results published by Rupp and Dress show the influence of crystal thickness and wavelength on the transmitted beam intensity versus time. However, there is no investigation of possible effects due to variations in the input angle of the beam or changes in the input intensity. The input angle and intensity are of interest for this research because they are key input parameters for two-wave coupling. The test procedures described in the next section were used to investigate the effects of variations in input beam angle and intensity on transmitted intensity versus time. Test conditions that result in maximum steady-state intensity transmission should be optimum for reducing the pump beam power lost to beam fanning.

3.3 *Equipment and Procedure*

Beam fanning test data was collected using the set-up shown in Figure 9. An uncollimated helium-neon laser with 6 mW maximum output power was used to illuminate the 1.5 mm diameter circular aperture. The laser output was horizontally polarized. Since the crystal c-axis was parallel to the input polarization, the input

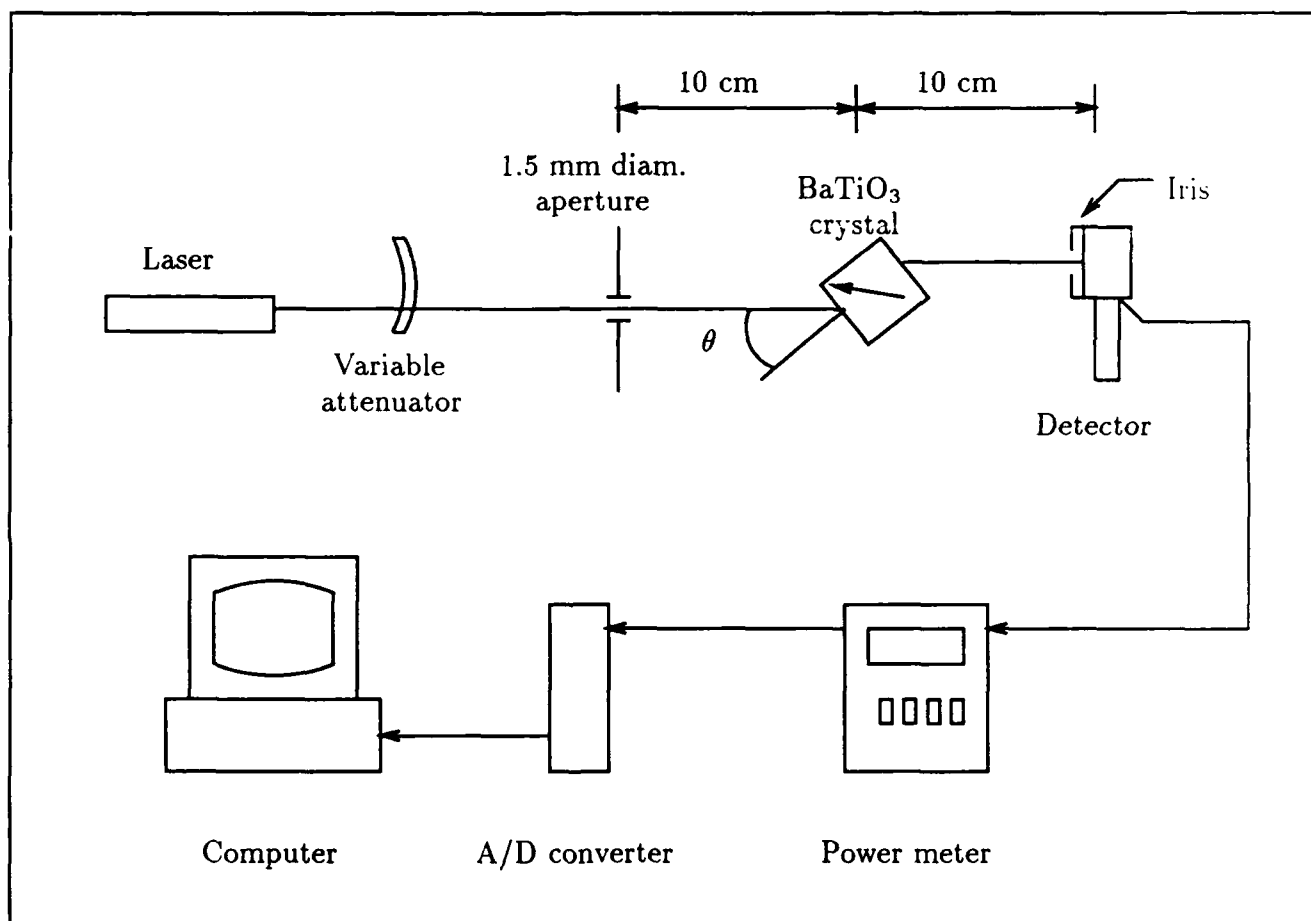


Figure 9. Beam Fanning Test Set-up

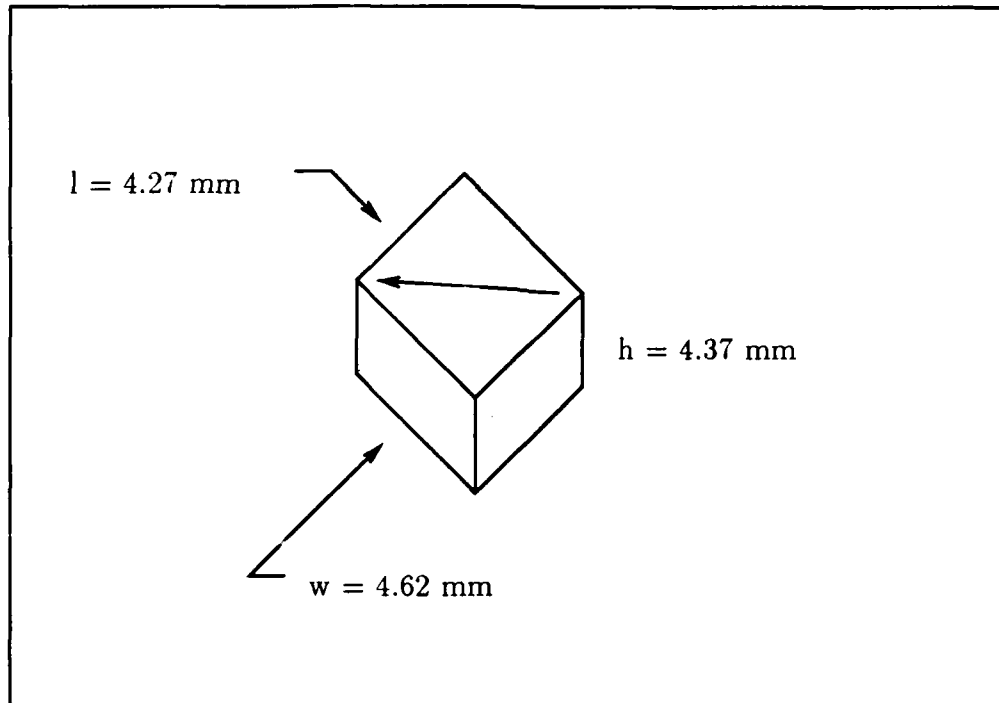


Figure 10. Dimensions of crystal #115-F

beam was extraordinarily polarized with respect to the crystal axes. This was the condition for maximum gain in BaTiO_3 and thus, maximum beam fanning. The 1.5 mm input beam diameter was chosen to allow transmission of the entire beam through the back surface of the crystal, provided the entrance angle, θ , was less than 40 degrees in either direction. A variable attenuator allowed 25, 50, and 75 % reductions of the intensity (or power) incident on the crystal.

The crystal used for all tests in this chapter was a 45°-cut BaTiO_3 crystal (#115-F). The dimensions of the crystal were as shown in Figure 10. Crystal #115-F was mounted on a rotating platform that allowed variation and direct measurement of the input beam angle. θ was defined as the external angle between the input beam and the normal to the front surface of the crystal. Clockwise rotations of the crystal were recorded as positive θ values. θ was varied from +40° to -20°.

An iris placed over the power meter detector allowed measurement of only

the transmitted beam power (i.e. - beam fanning energy was blocked). The analog voltage output from the power meter was connected via an A/D converter to allow digital recording of voltage versus time. A Computer- based Oscilloscope and Data Acquisition System (or CODAS) software package featuring a start/stop data recording function was used to monitor and record the test data. Prior to collection of each set of CODAS data, the input beam was blocked and the crystal was illuminated with a 21 mW incoherent light source for approximately one minute to erase any residual index gratings remaining in the crystal.

3.4 Results

Initial observations of the transmitted irradiance pattern of a single beam revealed that reduction of the input beam diameter dramatically reduced the amount of beam fanning. The fanning of a 1.5 mm diameter beam was much less than the scattering produced by an input beam that illuminated the entire entrance face of the crystal. The observed reduction of beam fanning with decreasing input beam diameter agrees with the findings of Moore and Walters, who observed an increase in asymmetric scattering with an increase in beam size for a constant power (17:1809).

Data plots of transmitted intensity versus time were created by converting CODAS voltage data files to lotus data files, and then using Symphony spreadsheet software to process and plot the data. Calibration tests, in which the CODAS voltage was recorded for a constant input power incident on the detector, were performed to determine the linear coefficients relating CODAS voltage to power displayed on the meter. The calculated power values were then divided by the area of the circular aperture to determine intensity values. Separate calibration tests were required for each meter range used during testing.

A typical transmitted intensity curve for an input intensity of 2.1 mW/mm^2 and $\theta = 0$ is shown in Figure 11. The beam entered the crystal at time $t = 2$ seconds, and the transmitted intensity appeared to decrease exponentially, as per Equation 5,

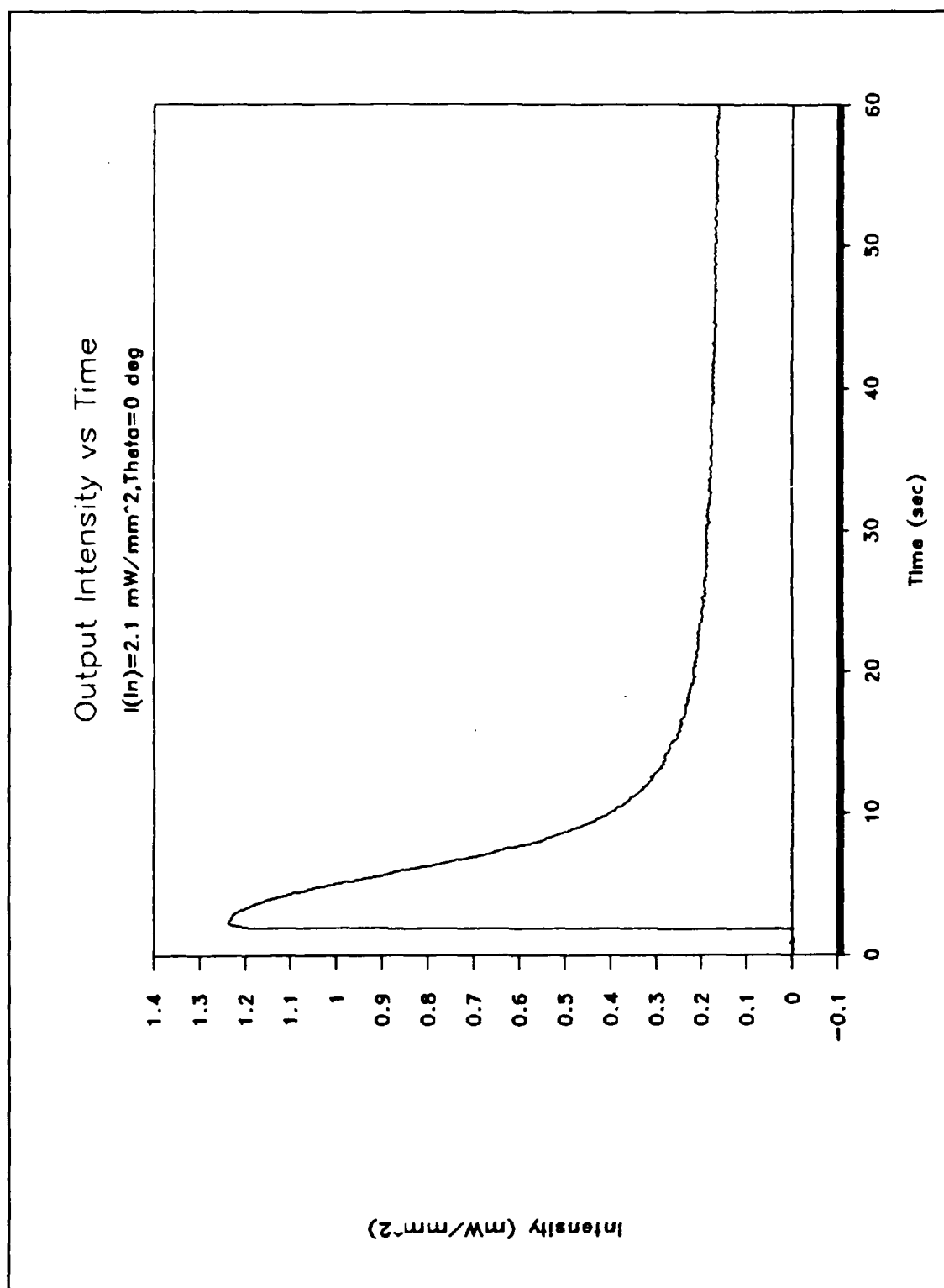


Figure 11. Transmitted Intensity versus Time for $\theta = 0$

until a steady-state value of 0.2 mW/mm^2 was reached. Partial absorption and reflection of the input beam resulted in a peak transmission of approximately 65 % of the original input intensity. Using Fresnel equations (10) for reflection losses at the front and back crystal faces, a transmission of 67 % of the input intensity was calculated. Beam fanning reduced the transmission of the input beam to approximately 10 % of the input intensity.

Transmitted intensity versus time curves for various input angles are shown in Figure 12. An input angle of +20 degrees resulted in the smallest steady-state pump depletion due to beam fanning. The largest pump depletion for the angles tested occurred at $\theta = -20$ degrees. No conclusions could be drawn that relate the observed results of fanning versus input angle to existing beam fanning or two-wave coupling theory.

The test curves in Figure 13 show how transmitted intensity versus time varies with input intensity, I_{in} . The percentage of pump energy lost to beam fanning appears to decrease as the input intensity decreases. Although the depletion percentage drops for decreasing input intensity, a larger input intensity will obviously provide more energy for two-wave coupling gain.

During testing, the transmitted intensity was found to be a function of the input position on the crystal face. Transmitted power versus time curves for three different input positions on the entrance face were generated using the same basic beam fanning test set-up described previously. The input power for each beam was 3.65 mW (irradiance of 2.1 mW/mm^2). The entrance angle for each input beam position was zero degrees (i.e. - the input beams were all normal to the crystal entrance face). Entrance positions for each beam are shown in Figure 14. Beam B was approximately centered on the input face of the crystal. Beam A entered the crystal 1.0 mm left of beam B, and beam C was 1.0 mm to the right. Since the diameter of each beam was 1.5 mm, all three beams were completely contained inside the crystal (i.e. - the beams did not reflect off the sides of the crystal until

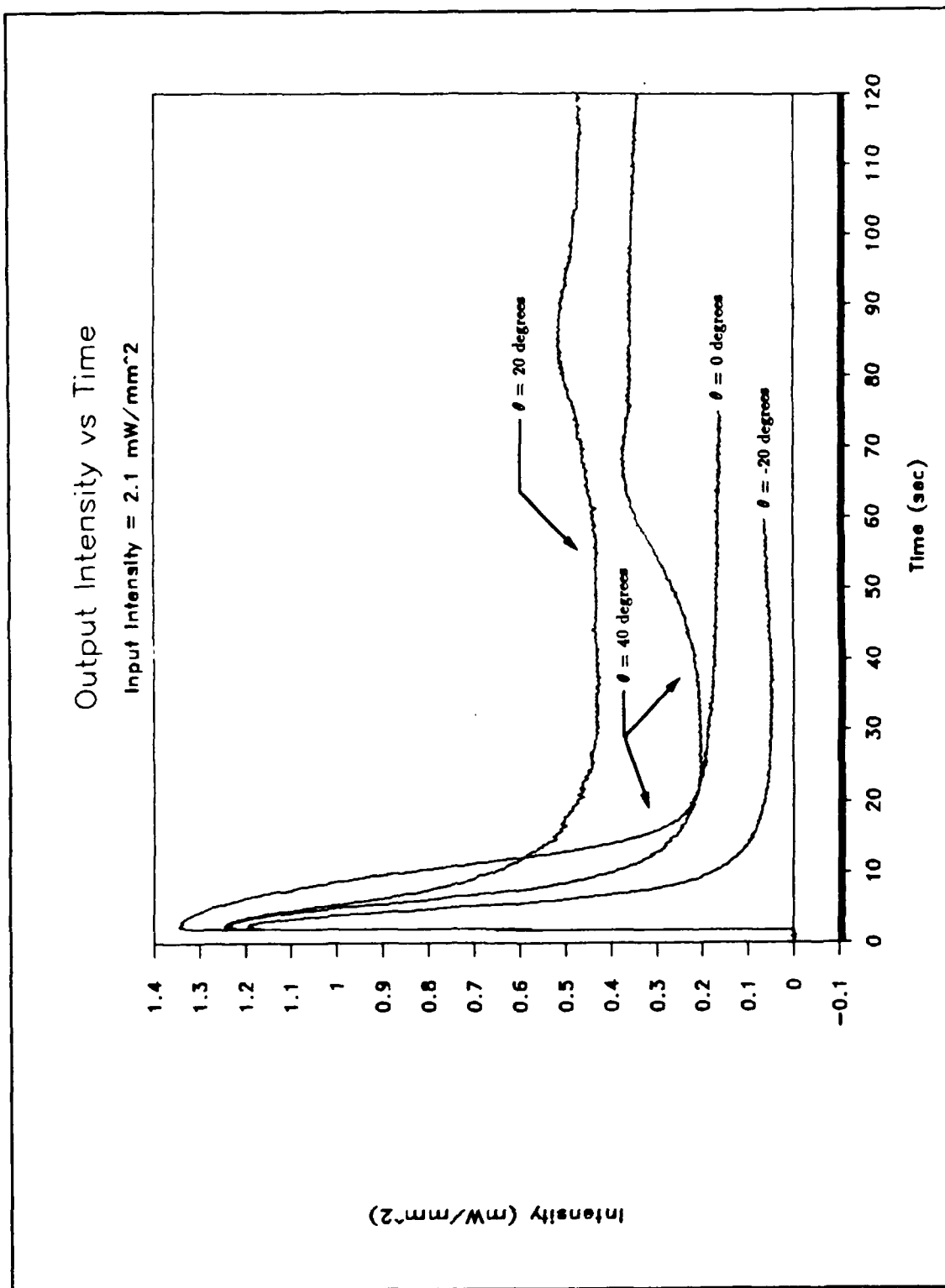


Figure 12. Transmitted Intensity versus Time for Various Entrance Angles

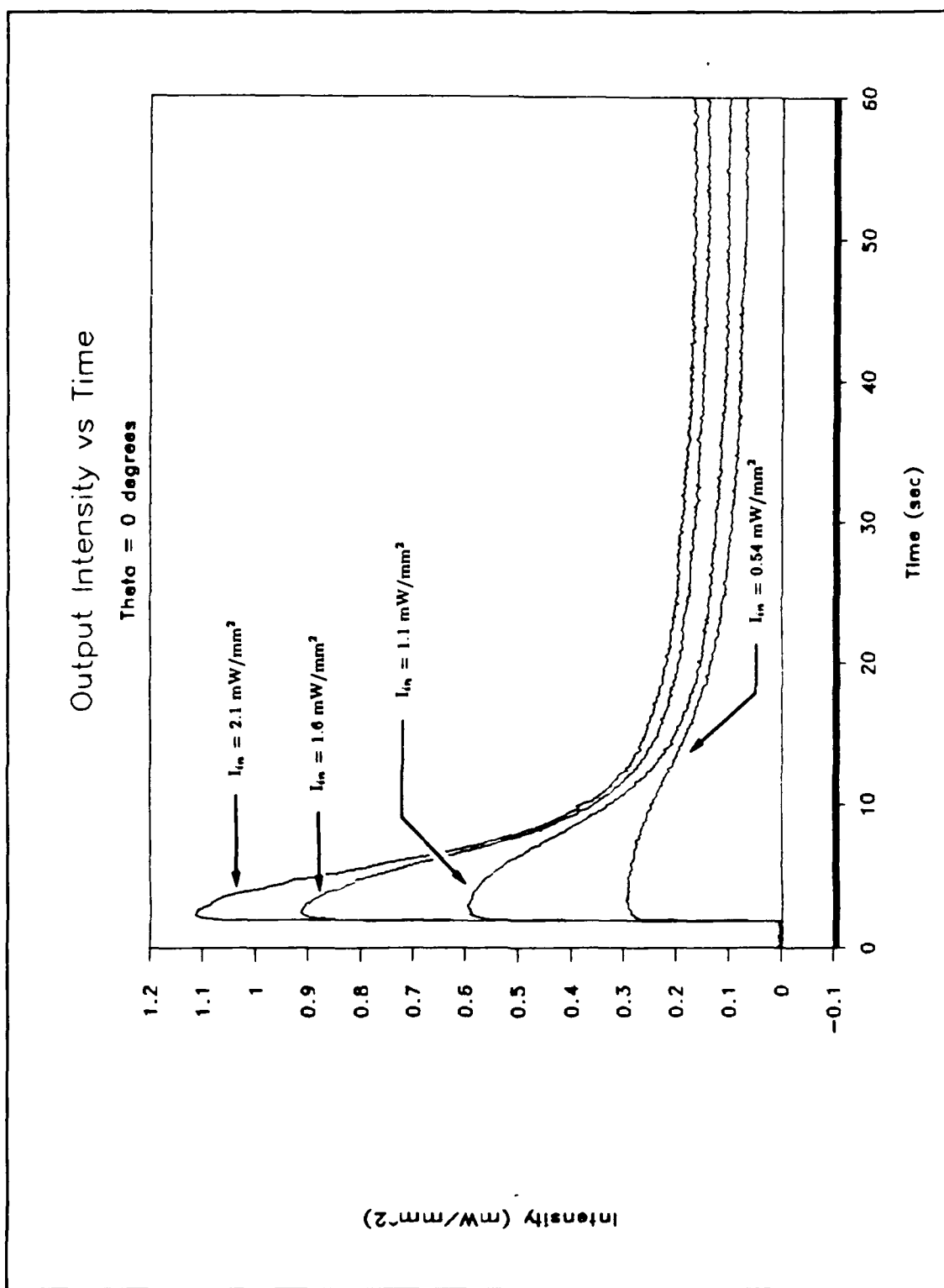


Figure 13. Transmitted Intensity versus Time for Various Input Intensities

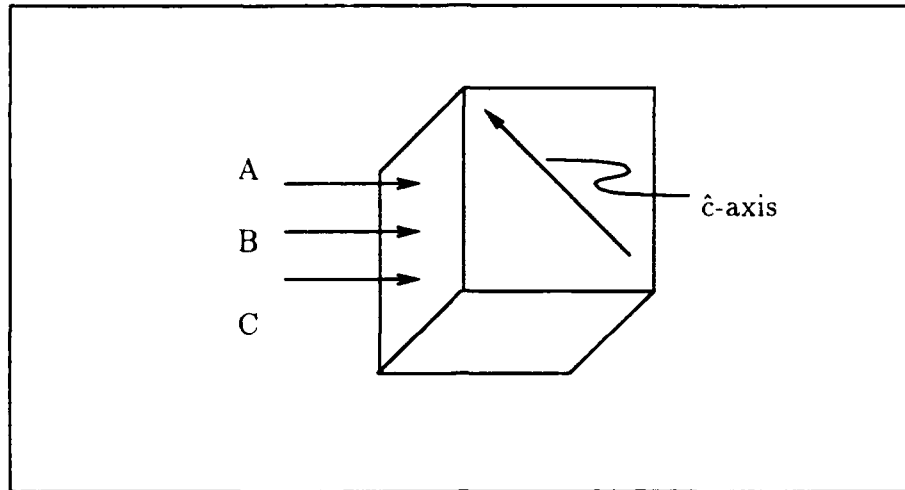


Figure 14. Beam Fanning Input Beam Positions

beam fanning occurred). Figure 15 shows the transmitted power versus time for each input beam position. The minimum transmitted powers (at $t = 50$ seconds) were 0.41 mW, 0.46 mW, and 0.60 mW for beams A, B, and C, respectively. Due to the complicated nature of the interaction between internally reflected beam fanning light and the input beam, no conclusions could be drawn from existing beam fanning or two-wave coupling theory.

In summary, three variables affecting loss of input beam energy to fanning were investigated: input angle, input intensity, and input position of the beam on the crystal. Plots of transmitted intensity (or power) versus time show how the variables affect depletion of the input beam caused by beam fanning. Transmitted intensity was most sensitive to variations in the input beam angle. An input angle of +20 degrees allowed the highest steady-state transmission for the input angles tested. In the next chapter, beam fanning is investigated in conjunction with two-wave coupling.

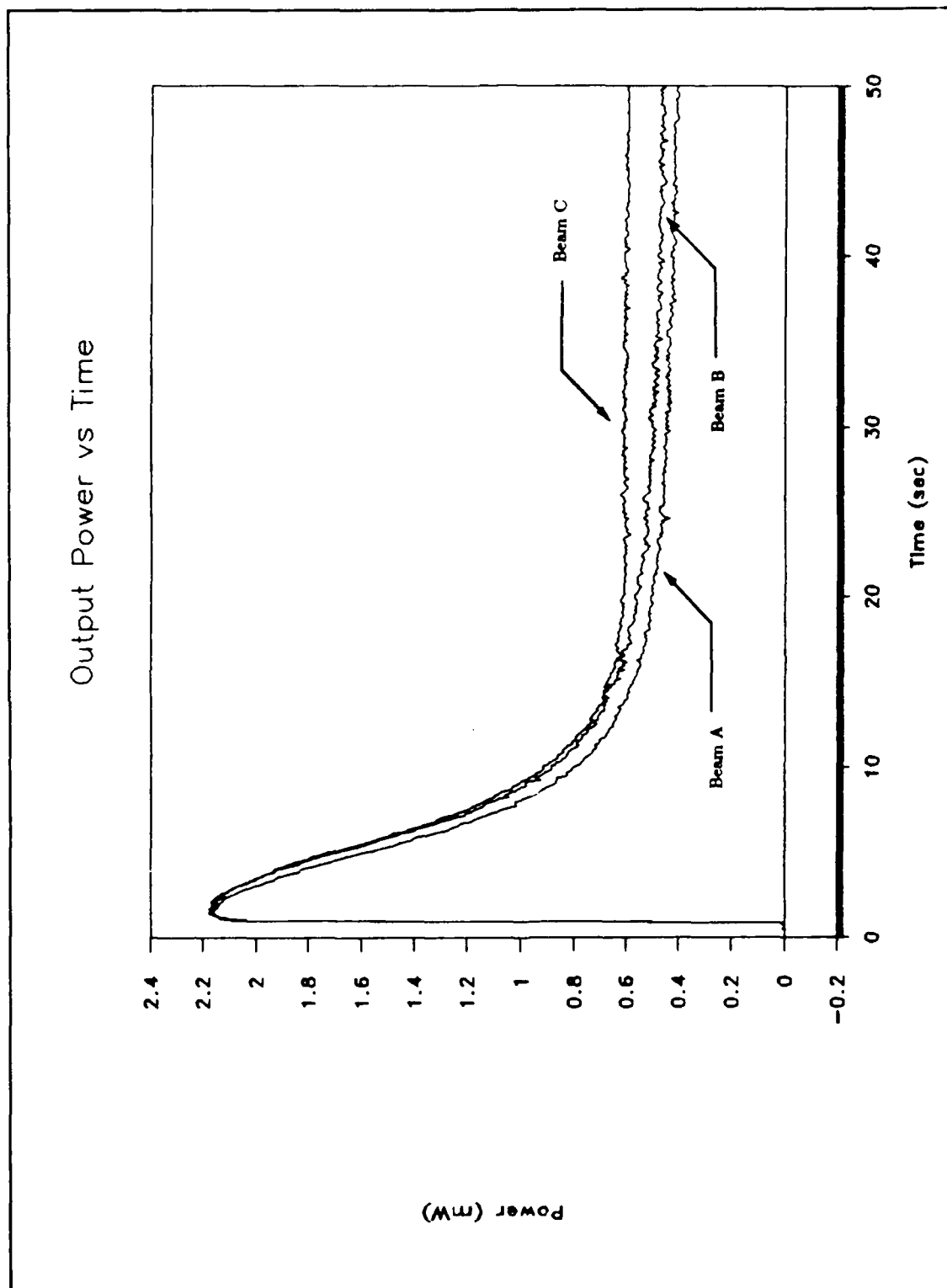


Figure 15. Transmitted Intensity versus Time for Various Input Positions

IV. Two-Wave Coupling Testing

4.1 Introduction

Beam fanning was discussed in the previous chapter because of its observed degradation of two-wave coupling gain. The topic to be discussed in this chapter is testing of 45°-cut BaTiO₃ crystals to determine and minimize adverse effects of beam fanning on two-wave coupling gain. A summary of the background theory related to the topic of discussion will be presented first. Then, the experimental set-up and procedures will be described. Finally, the test results will be presented and discussed.

4.2 Background Theory

Recall from Section 2.2 that the "effective gain", γ_o , was expressed by Günter as

$$\gamma_o = \frac{(1 + r) \exp(\Gamma d)}{1 + r \exp(\Gamma d)} \quad (6)$$

where $r = I_s/I_p$ is the ratio of the input signal beam intensity to the input pump beam intensity, Γ is the two-wave coupling exponential gain coefficient, and d is the interaction length of the two beams inside the photorefractive medium. This expression can be easily solved algebraically for Γ to yield

$$\Gamma = \frac{1}{L} \ln \left[\frac{G_o}{(1 + r) - r G_o} \right] \quad (7)$$

where G_o and L are the symbols used in place of γ_o and d in the two-wave coupling paper published by Fainman *et al.* (2:288). Fainman *et al.* presented calculated values of Γ versus input parameters related to the geometry of the two input beams. Two key input parameters were the angles β and θ shown in Figure 16. The angle 2θ is the angle between the pump and signal beams, and β is the angle between the \hat{c} -axis and the grating vector (the perpendicular to the bisector of the angle 2θ).

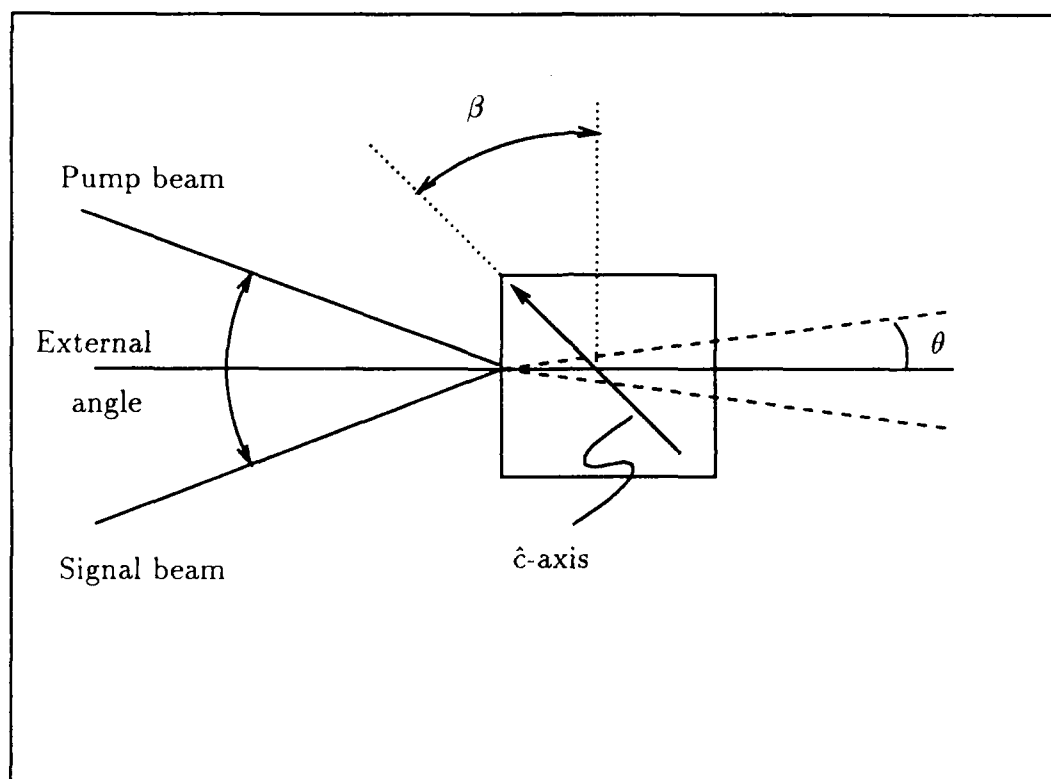


Figure 16. Two-Wave Coupling Input Geometry

Note that 2θ and β are measured between directions inside the crystal (i.e. - Snell's law must be used to convert external angles to internal angles and vice versa). Based on their mathematical models, and experimental results with z-cut BaTiO₃ crystals, Fainman *et al.* recommended a special 45°-cut crystal be manufactured and tested.

In Section 2.4 of the Summary of Current Knowledge, the results of two-wave coupling experiments (with 45°-cut BaTiO₃ crystals) published by Wilson and Ford *et al.* were discussed. Wilson investigated Γ values with θ (internal) of up to 3.5° and recommended testing of larger θ angles (25:67). Ford *et al.* presented an experimental plot of Γ versus θ for a 2.5 mm thick crystal. The highest Γ values (26 cm⁻¹) were achieved with a θ of 8 degrees using the thinner crystal (8). The test procedures described in the following section were accomplished to determine the maximum achievable gain for two different 45°-cut BaTiO₃ crystals, and to investigate the effects of beam fanning on two-wave coupling gain.

4.3 Equipment and Procedure

The experimental set-up used to collect two-wave coupling data is shown in Figure 17. A Coherent INNOVA 100-20 Argon Ion laser was used to produce the two input beams used for two-wave coupling. The laser was operated in a single longitudinal mode at a wavelength of 514.5 nm. Single mode operation provided a longer laser coherence length (than multiple mode operation) that was desirable for two-wave coupling.

Three devices were used to control the laser output characteristics. A continuously variable attenuator (CVA) was used to precisely control the Argon laser output, and thus, the power of the pump beam transmitted through aperture 1. The polarization rotator (PR) was adjusted to produce a horizontally polarized output beam. Therefore, the pump and signal beams were both extraordinarily polarized. A spatial filter/collimator (SFC) was used to expand the beam to a 2 inch diameter.

The expanded beam was split into two beams via a 50/50 beamsplitter. The

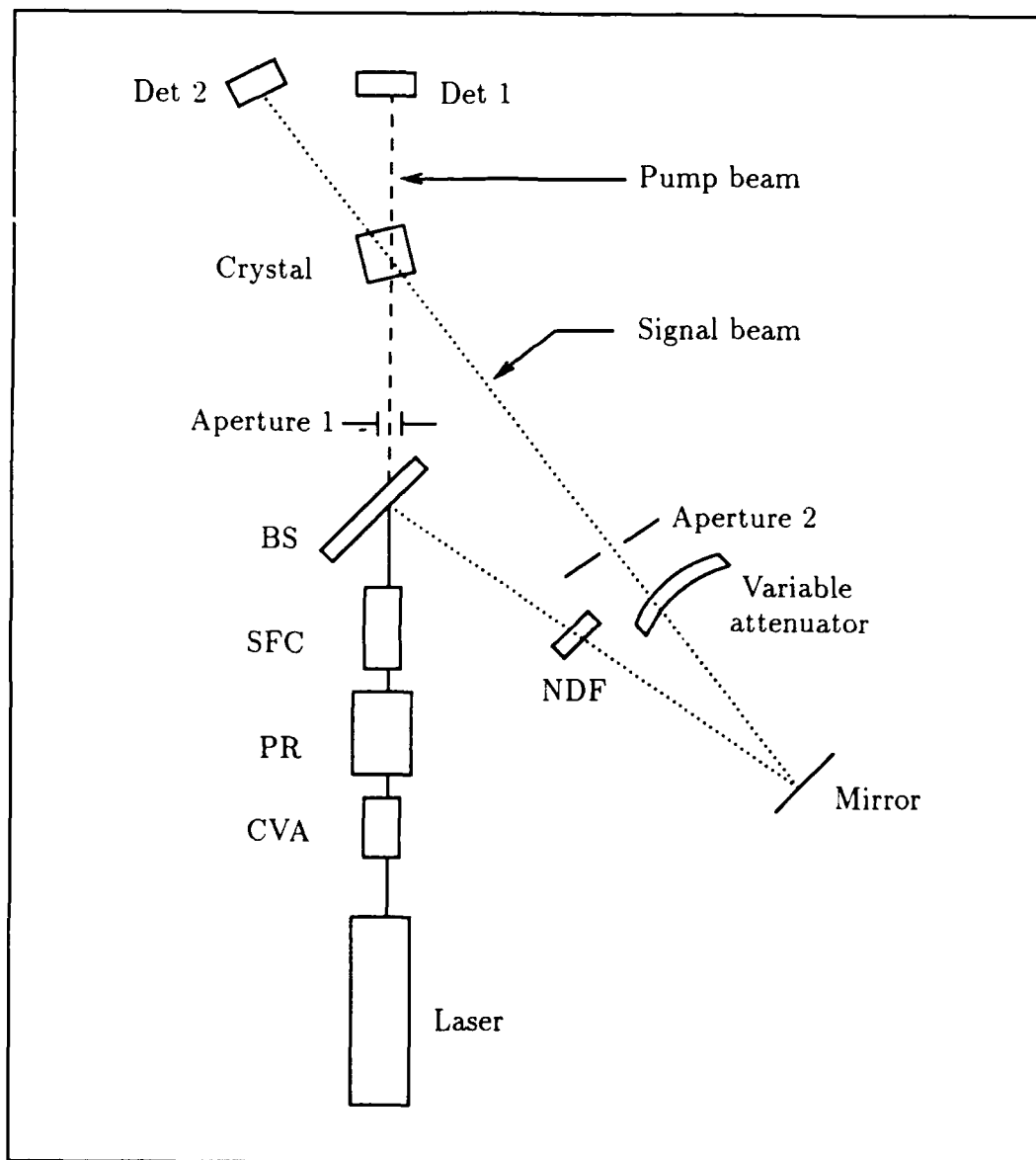


Figure 17. Two-Wave Coupling Experimental Set-up

pump beam was the portion of the beam transmitted through the beamsplitter. Aperture 1 was a 3.0 mm diameter circular aperture (positioned 5 inches in front of the crystal input face) used to restrict the size of the pump beam entering the crystal. The pump beam size was restricted to reduce fanning of the pump beam as discussed in Section 3.4. The portion of the light reflected by the beamsplitter was used for the input signal beam. The signal beam power, through aperture 2, was controlled using a variable attenuator disk. Neutral density filters were inserted between the beamsplitter and the signal beam mirror when greater attenuation (than the disk could provide) was required. Aperture 2 was a 1.5 mm diameter circular aperture positioned 9.5 inches from the crystal input face.

Two 45°-cut BaTiO₃ crystals manufactured by Sanders Associates were used during testing. The crystal serial numbers were 115-F and 133-E. The dimensions of crystal 115-F were $l = 4.27$ mm, $w = 4.62$ mm, and $h = 4.37$ mm as shown in Figure 10. Crystal 133-E was a 5.5 mm cube. A third 45°-cut crystal (serial # 163-A) was excluded from the test results due to a peculiar bright line observed in the fanning pattern (produced by a single input beam).

Precise control of the input angles and positions of the input beams were required to achieve repeatable test results. Figure 16 shows the crystal input beam geometry in detail. The external angle between the pump and signal beams outside the crystal was approximately 40 degrees. This corresponds to an internal angle, θ , of approximately 8 degrees. The value for θ was chosen based on the results of Ford *et al.* (8), as discussed in the previous section. The input positions of the pump and signal beams were adjusted to allow maximum overlap of the two beams inside the crystal. Figure 18 shows the relative positions of the two beams and the overlap region.

During image amplification tests (to be discussed in the next chapter), two amplified output signal beams were observed for a single input signal beam. The second output beam was due to amplification of a double reflection of the original

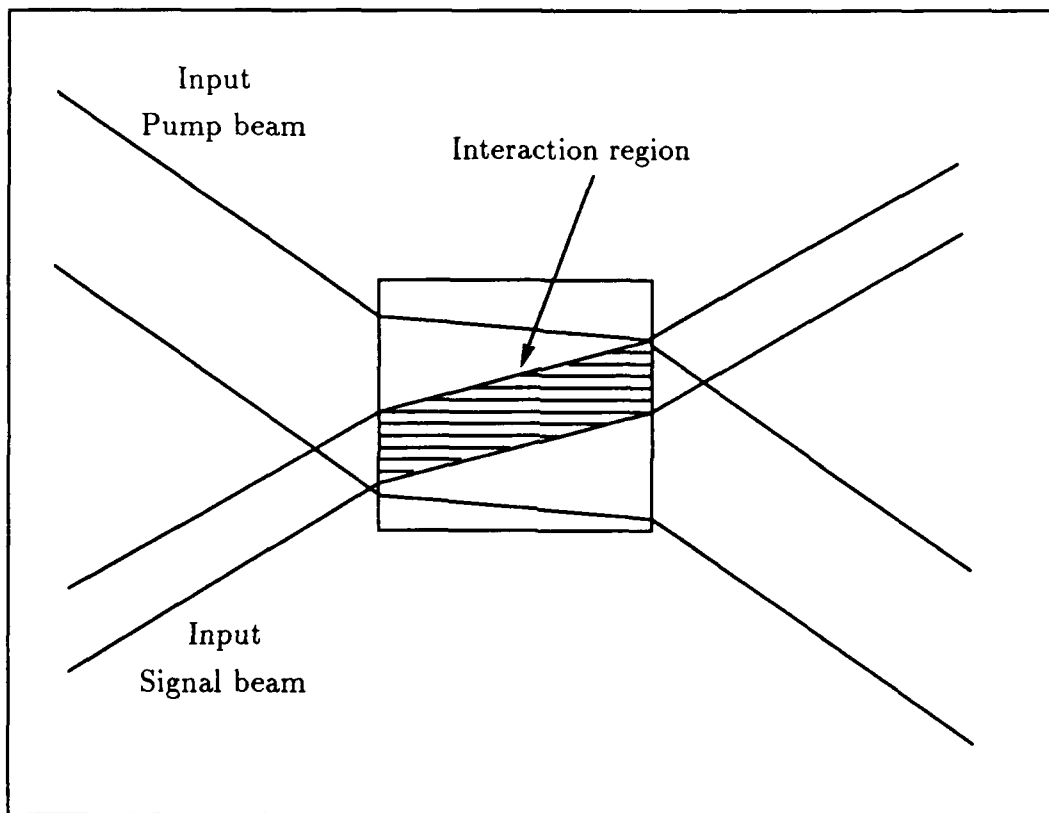


Figure 18. Pump and Signal Beam Positions Inside the Crystal

input beam inside the crystal. Detector 2 was placed 17.5 inches behind the crystal exit face, and was covered with a variable circular iris adjusted to a 3.0 mm diameter. The iris diameter and the position of the detector were chosen so that only the power of the amplified input beam was recorded (i.e. - the secondary beam power was blocked by the iris diaphragm). The 17.5 inch distance was adequate to ensure complete separation between the two output signal beams. Note that no iris was placed over the pump beam detector.

The voltage output from the pump and probe beam detectors was recorded using CODAS software and the same procedures detailed in Section 3.3. The 21 mW incoherent light source was used to erase residual gratings before each test, except for one test involving pre-fanning of the pump beam prior to signal beam transmission. Input pump beam powers of 10, 1.0, and 0.1 mW were used throughout the testing. Signal beam powers were varied from 1.0 mW to 0.001 mW depending on the test and the input pump beam power. The angle β was approximately 45 degrees for all tests except for one series of tests where β was varied between 35 and 49 degrees. The angle θ was fixed at 8 degrees for all tests.

4.4 Results

Data plots of output power versus time were created using CODAS voltage data files (obtained with the set-up discussed in the previous section) and Symphony spreadsheet processing as discussed in Section 3.4. Unless specified otherwise, the following discussions and results are for crystal 115-F and a β , the \hat{c} -axis to grating vector angle, of 45 degrees.

The amount of pump power fanned in the direction of the amplified signal beam was measured for all three pump powers used during two-wave coupling testing. With the signal beam blocked, the pump beam was allowed to completely fan out. The maximum pump beam fanning powers measured at detector 2 were 0.81, 0.16, and .002 μ W for input pump powers of 10, 1.0, 0.10 mW, respectively. All three of the

pump fanning powers were at least two orders of magnitude lower than the lowest steady-state signal powers recorded for each pump power. Thus, the signal 'noise' due to fanning of the pump beam was considered to be insignificant for all pump powers tested.

A typical plot of pump and signal output power versus time is shown in Figure 19. The initial input pump power, $P_p(0)$, through aperture 1 was 10 mW. The initial input signal power, $P_s(0)$, through aperture 2 was 1.0 mW. Both the pump and signal beams entered the crystal at time, $t = 0.5$ sec. The peak signal output power of 2 mW occurred at approximately, $t = 0.8$ sec. As reported by Wilson, the signal output reaches a peak value and then decays (apparently due to beam fanning). This is in contrast to a steady-state peak value observed with the 'lower gain' z-cut BaTiO₃ crystals.

Figure 20 shows the pump beam output for, $P_p(0) = 10$ mW and no signal beam. Notice the higher output pump peak power and the slower decrease in power compared to that for the two-wave coupling curve in Figure 19. The transmitted pump power curves from Figure 19 and Figure 20 are superimposed in Figure 21. The two curves are practically indistinguishable except for the time period between $t \approx 0.5$ sec and $t \approx 1.5$ sec. The pump power is depleted faster during two-wave coupling than during single beam fanning. The final pump depletion (i.e. - $t > 6$ sec), however, appears to be the same for beam fanning and two-wave coupling. The observations regarding comparison of two-wave coupling and beam fanning transmitted pump beam powers were not unique to a pump power of 10 mW. Similar trends were observed with 1.0 and 0.1 mW pump beam powers.

Figures 22 and 23 show output pump and signal powers for $P_p(0) = 10$ mW, and $P_s(0) = 0.10$ mW and 0.01 mW, respectively. Reduction of the input signal beam power increases the time until the output signal power reaches a peak, and decreases the peak output power, as expected. However, notice that although the input power has been reduced by a factor of 10, the peak signal output is reduced

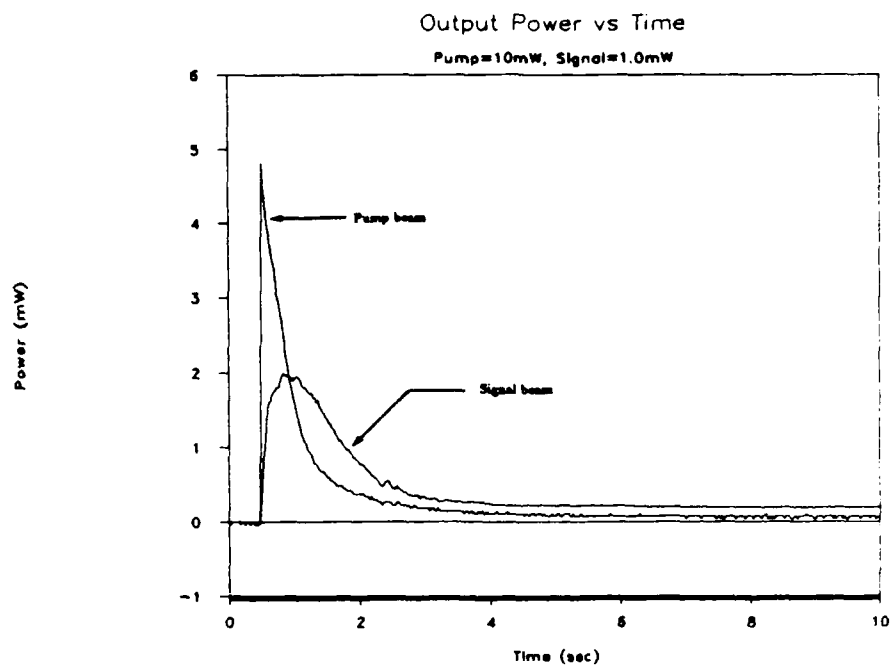


Figure 19. Output Power versus Time, $P_p(0)=10$ mW, $P_s(0)=1.0$ mW

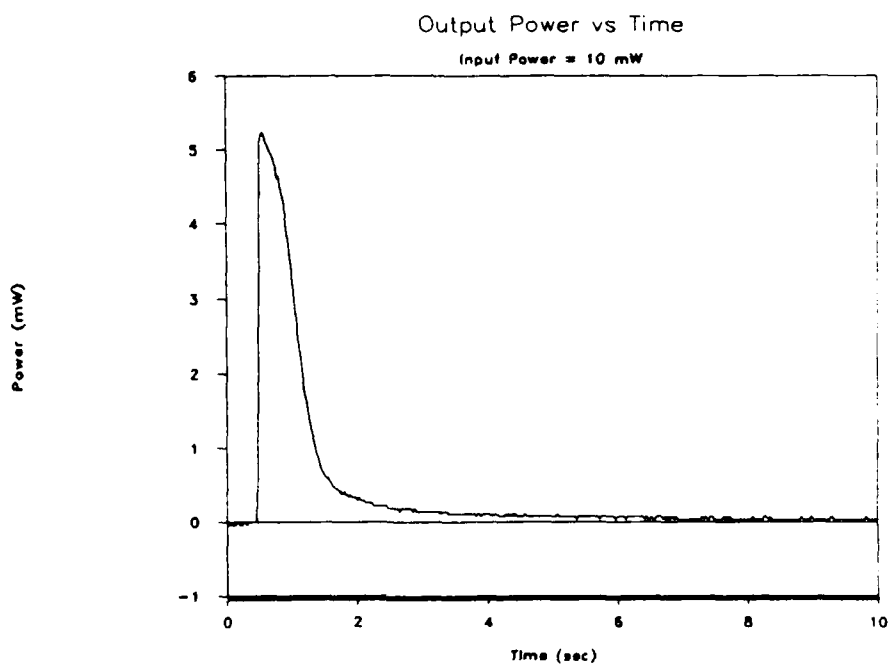


Figure 20. Pump Beam Output Power versus Time

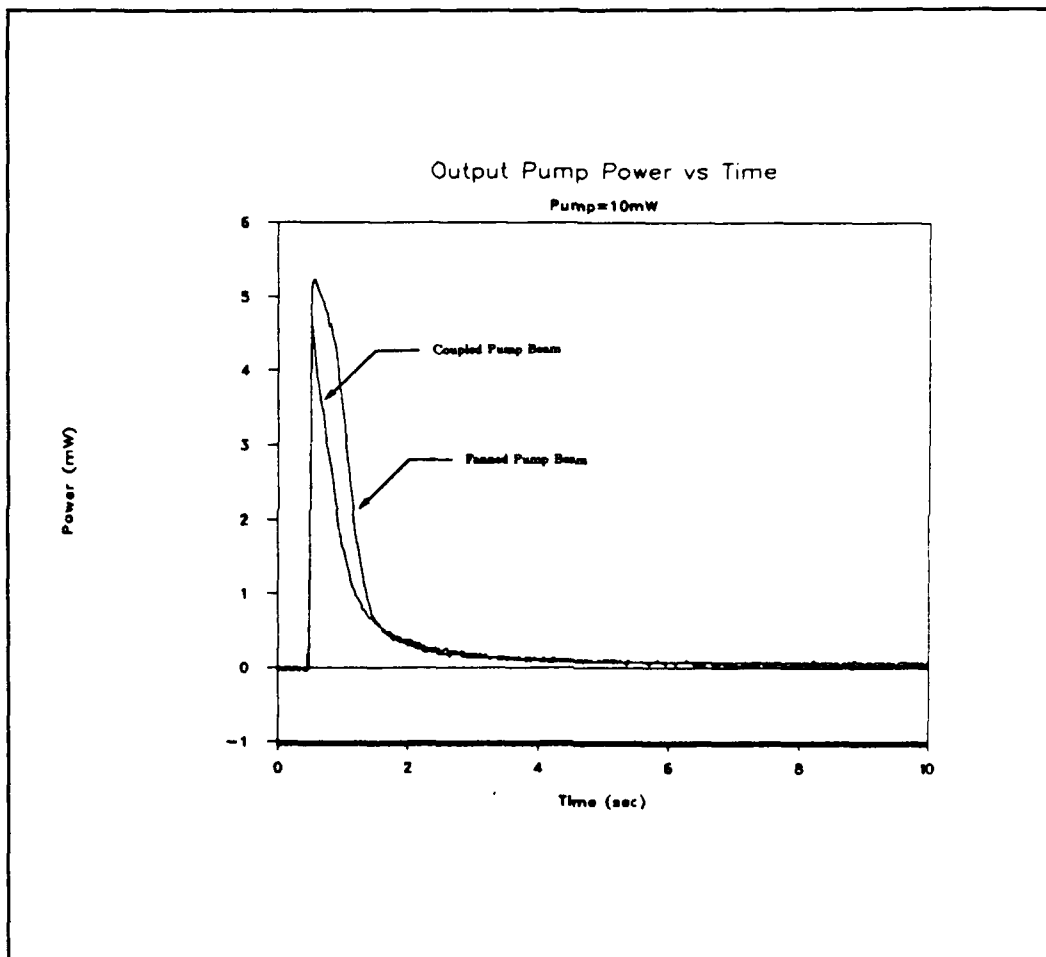


Figure 21. Transmitted Pump Power with and without an Input Signal Beam

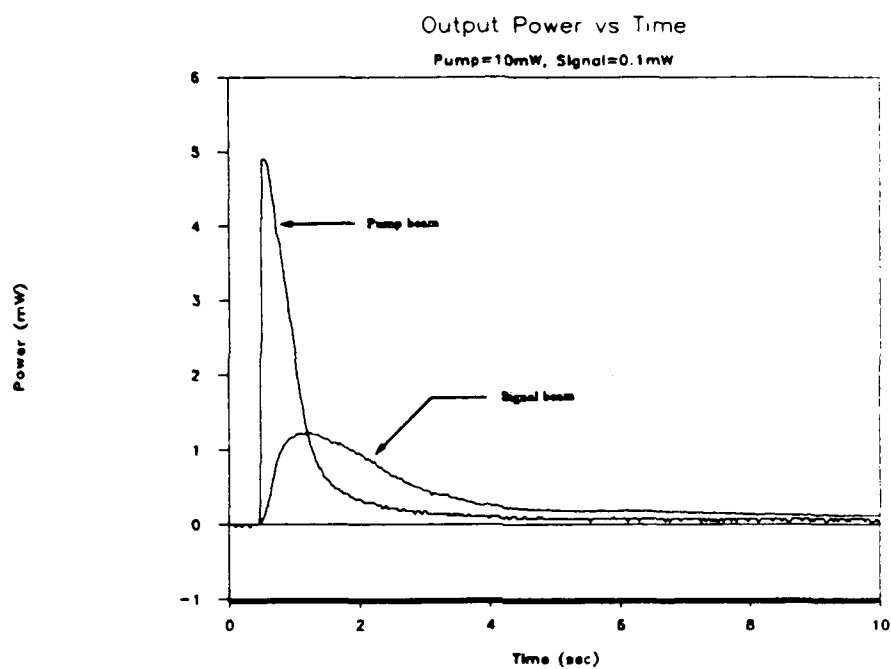


Figure 22. Output Power versus Time, $P_p(0)=10$ mW, $P_s(0)=0.10$ mW

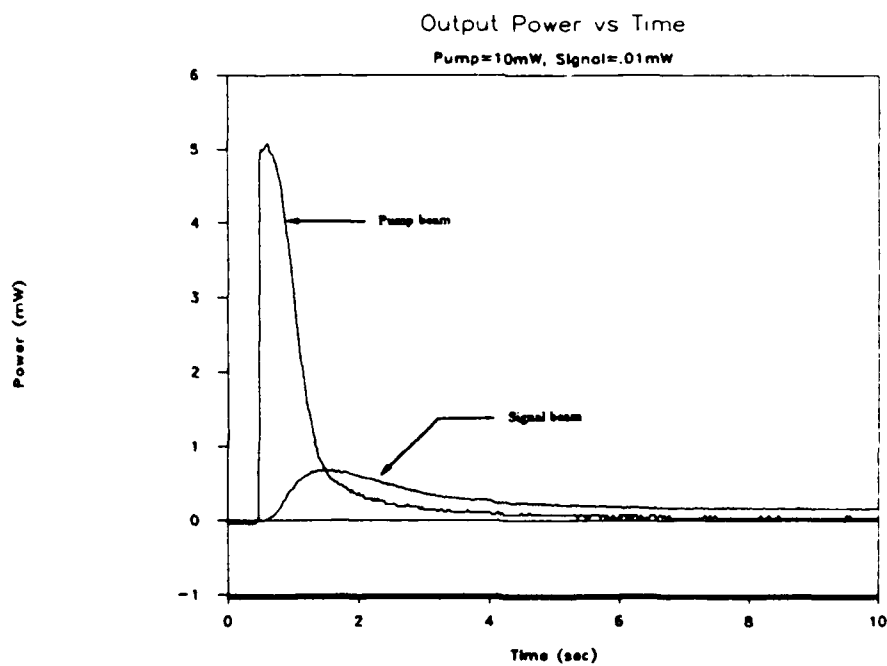


Figure 23. Output Power versus Time, $P_p(0)=10$ mW, $P_s(0)=0.01$ mW

by a smaller factor. Thus, the signal input/output ratio, or gain, increases as $P_s(0)$ decreases (for a constant pump power). In addition, notice that the lower the input signal power, the closer the pump curve resembles the single beam fanning curve in Figure 20.

The next set of plots show only the signal beam output powers resulting from two-wave coupling tests. Figure 24 shows signal beam output powers for $P_p(0) = 10$ mW. The input signal powers were 1.0 mW, 0.10 mW, 0.01 mW, and 0.001 mW. Figures 25 and 26 are similar plots for $P_p(0) = 1.0$ mW and 0.10 mW, respectively. The first two plots show similar signal amplification curves, especially for the input pump to signal ratios of 10 and 100. Note that the vertical axis of each plot is an order of magnitude less for each order of magnitude reduction in the pump power. The output signal curves appear much different for the $P_p(0) = 0.1$ mW pump than for the other two pump powers. The output signal curves for $P_s(0) = 0.033$ mW and 0.001 mW show steady-state gains equal to the peak gain. Beam fanning of the 0.1 mW pump beam did occur. However, the pump beam fanning does not appear to have caused reduction of the output signal beams. A lower pump power limit seems to have been reached, below which, the signal beam is unaffected by beam fanning.

Rotation of the input beam polarizations was investigated as a way to produce steady-state gains equal to the peak gain. Simultaneous pump and signal beam rotations of 45 degrees clockwise and then 45 degrees counter-clockwise were tested. Steady-state gains equal to the peak gain were observed for both the clockwise and counter-clockwise rotations. In addition, the steady-state gains achieved with 45 degree polarization rotation were 2 to 3 times higher than the steady-state gains achieved with extraordinarily polarized pump and signal beams. However, the polarization of the output signal beam was elliptical (or circular) due to the birefringence of the crystal. Since image amplification in Wilson's proposed Optical Associative Memory architecture requires no rotation of the output image polar-

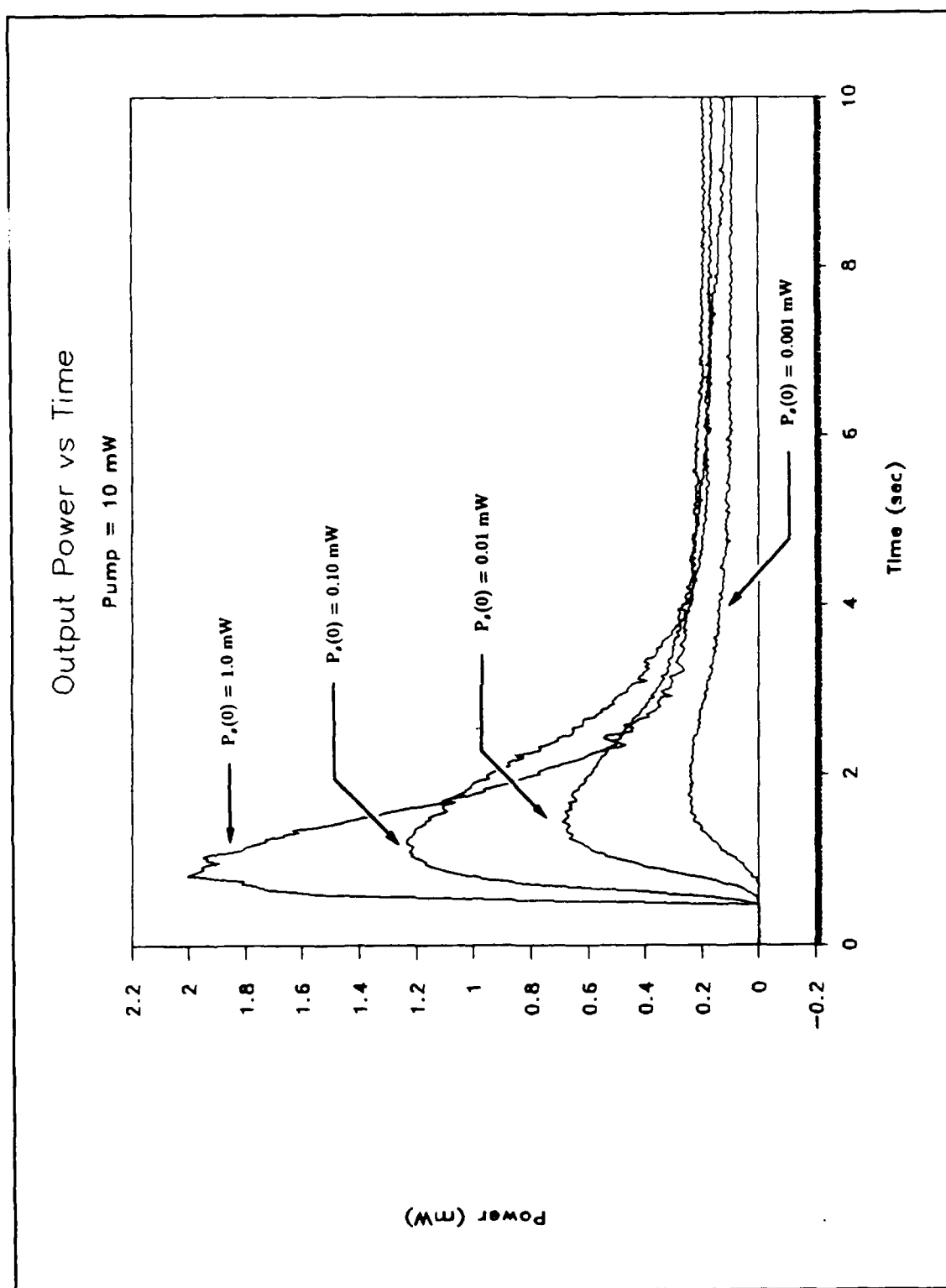


Figure 24. Signal Beam Output Power versus Time for a 10 mW Pump

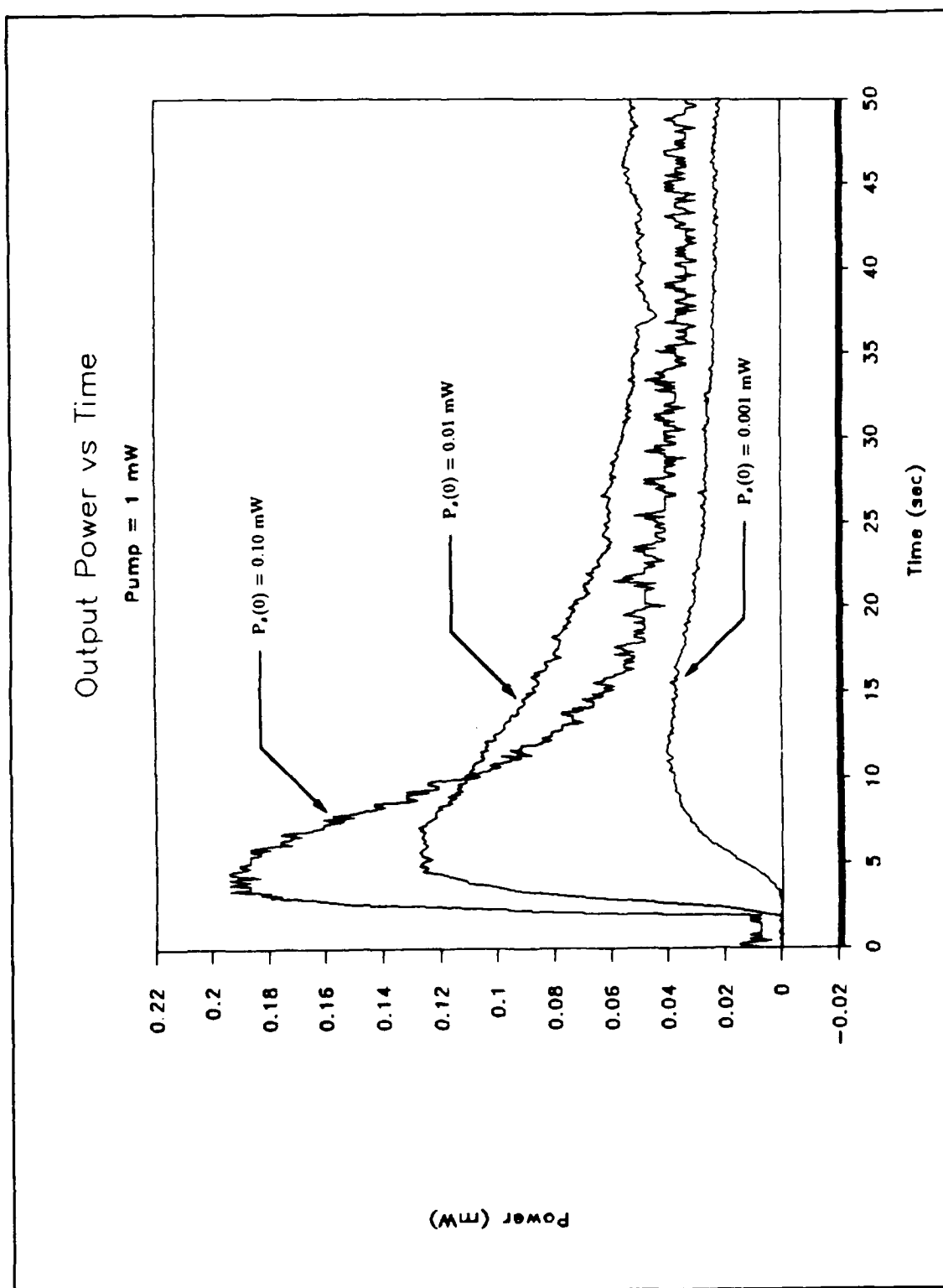


Figure 25. Signal Beam Output Power versus Time for a 1.0 mW Pump

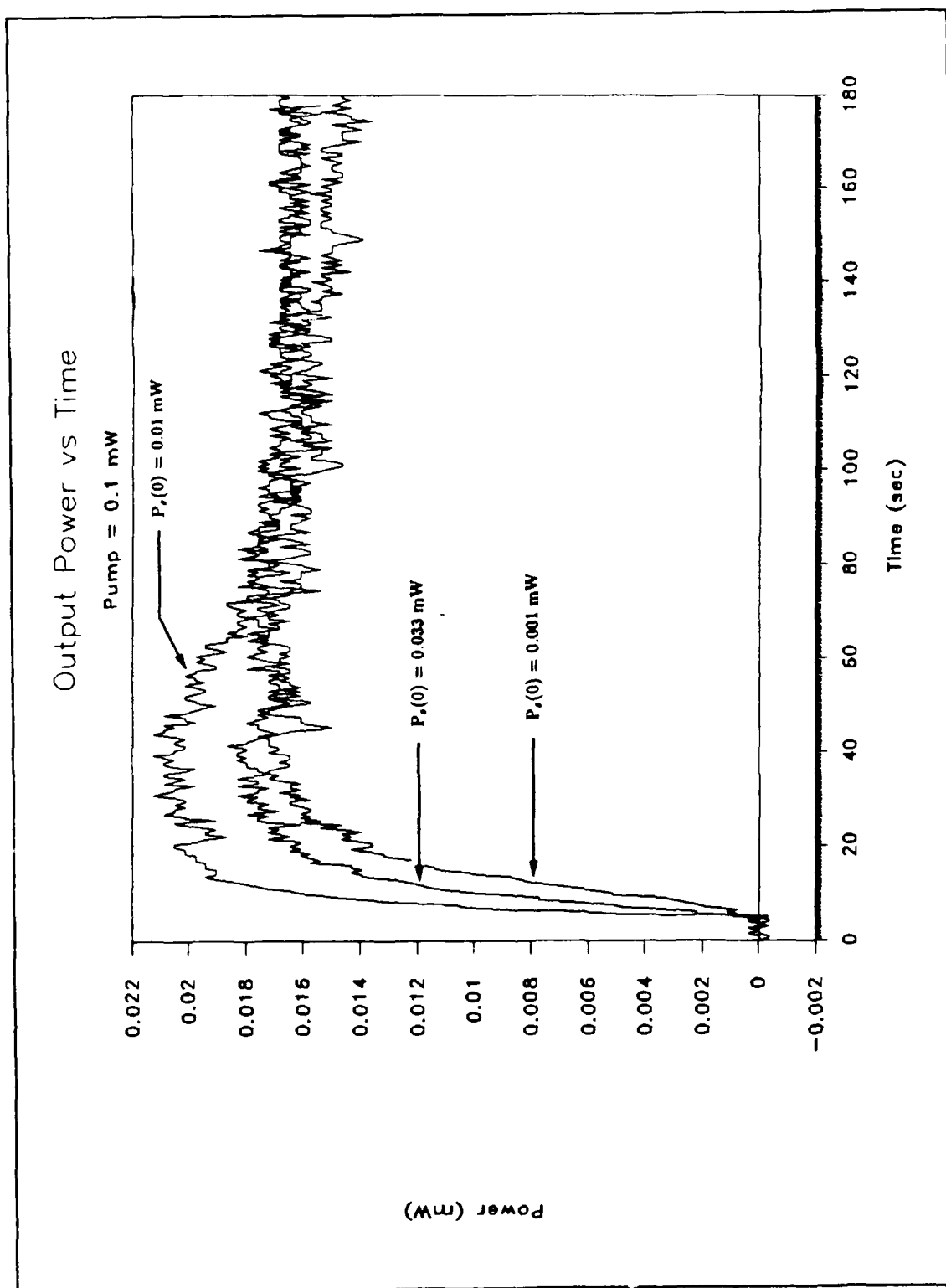


Figure 26. Signal Beam Output Power versus Time for a 0.1 mW Pump

ization, tests investigating input polarization rotation were not pursued further. A waveplate located behind the crystal that rotates the output polarization back to the original input polarization may be a solution to the problem. However, the loss due to transmission through the waveplate may cause unacceptable reduction of the total output gain. Figures 27 and 28 show output power versus time for extraordinary input polarization and 45° clockwise rotation from e-polarization, respectively. The input powers were $P_p(0) = 1.0$ mW and $P_s(0) = 0.1$ mW. In addition to the steady-state signal output, notice the decrease in pump power lost due to beam fanning for the 45° clockwise rotation of the polarization. In Figure 28, the steady-state output signal beam power is approximately 0.1 mW. Since the input signal power was 0.1 mW, there appears to be no amplification. However, the signal beam output power without the pump beam was 0.04 mW due to reflection losses at the crystal input and exit faces. Thus, two-wave coupling gain was demonstrated for polarization rotation of the input beams even though there was little total system input to output gain.

Calculation of realistic Γ values for the two-wave coupling tests performed were unsuccessful. Γ values calculated using the experimental set-up described in Section 4.3 resulted in imaginary numbers because the product of rG_o was greater than $(1 + r)$ in the denominator of Equation 7. The unrealistic Γ values prompted an investigation of the experimental set-up used to collect the two-wave coupling data.

The experimental set-ups used by Wilson and Ford *et al.* were slightly different from the set-up discussed in the previous section. Wilson used a rectangular shaped input pump beam, a circular signal beam of 2.0 mm diameter, and a circular iris of 1.5 mm diameter over the detector for all power measurements. Ford *et al.* used rectangular shaped pump and signal beams (to use as large a volume of the crystal as possible), and a 1 mm diameter iris over the detector for all power meter measurements. Both Wilson and Ford *et al.* measured initial pump and signal powers in front of the crystal entrance face for calculations of r in Equation 7. They also used

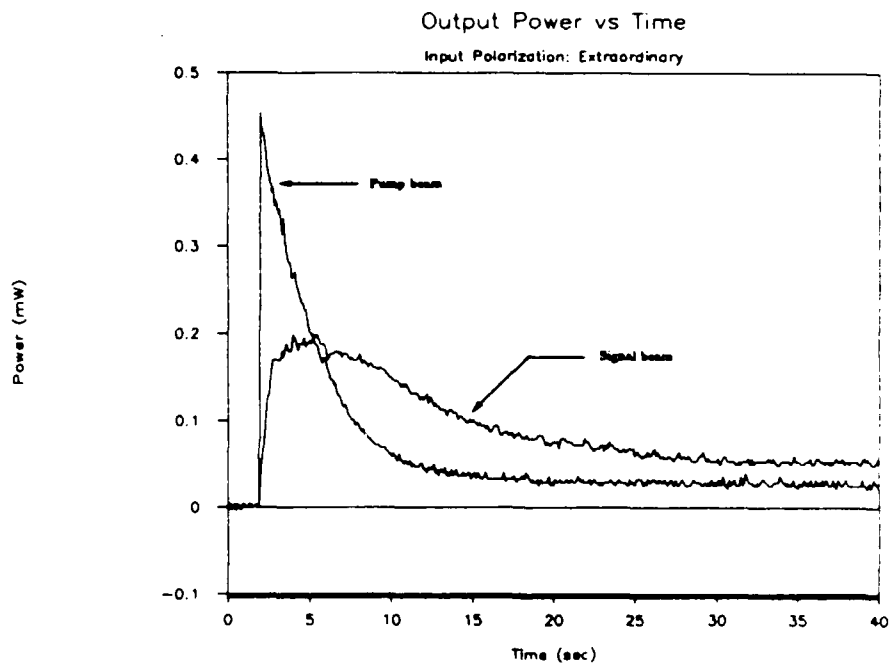


Figure 27. Output for Extraordinarily-polarized Input Beams

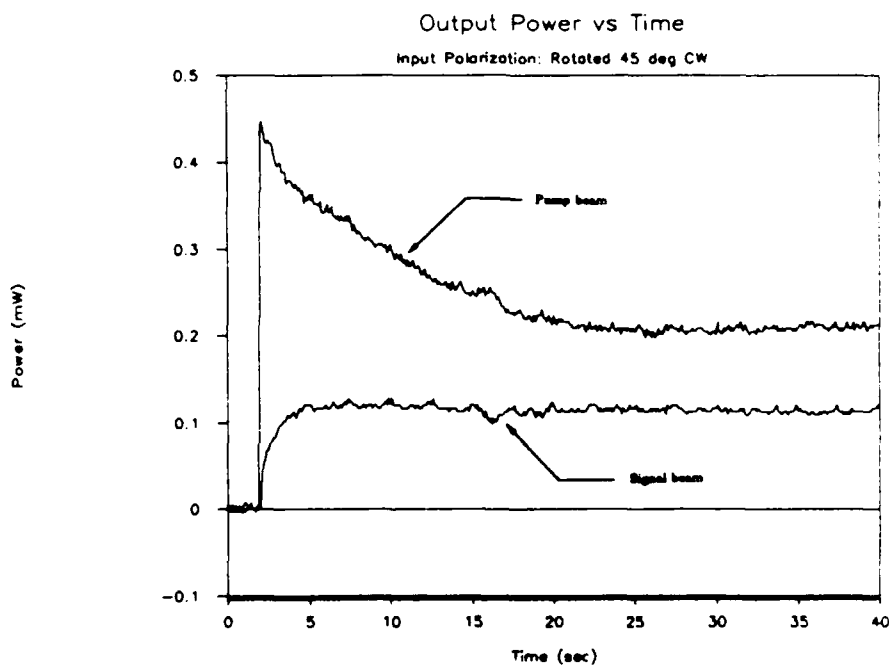


Figure 28. Output for 45° CW Polarization Rotation

the ratio of the peak output signal beam power (obtained via two-wave coupling), to the 'unpumped' transmitted signal beam power to calculate the effective gain, G_o .

Based on Wilson and Ford's set-ups, four methods for obtaining data to calculate r and G_o were tested. The positions of the power measurements used for the four methods are shown in Figure 29. The zeros inside the parentheses indicate values recorded without two-wave coupling (i.e. - prior to two-wave coupling). Note that the primes indicate powers measured behind the crystal. $P'_s(pk)$ was the peak output signal power recorded. In Method 1, r was calculated as follows

$$r = \frac{P_s(0)}{P_p(0)} \frac{A_p}{A_s} \quad (8)$$

where A_p and A_s were the respective areas of the pump and signal beams. The gain was calculated as $G_o = P'_s(pk)/P'_s(0)$. No iris was used over the power meter detector for the measurements of $P_s(0)$ and $P_p(0)$. An iris set to the diameter of the amplified signal beam was used for the $P'_s(0)$ and $P'_s(pk)$ measurements. Method 2 was identical to Method 1, except that a 1.5 mm diameter iris was placed over the detector for all power measurements. Methods 3 and 4 were the same as 1 and 2 respectively, except that $P'_s(0)$ and $P'_p(0)$ were used in place of $P_s(0)$ and $P_p(0)$ to calculate r . Γ was determined for each of the four methods with $P_p(0) = 1.0$ mW and $P_s(0) = 0.050$ mW. The resulting Γ 's were imaginary for all methods except number 4 ($\Gamma = 8.75$ cm⁻¹).

Although the two-wave coupling experimental set-up used in this thesis appears to be the cause of the imaginary Γ values, it is still unclear why such values occur for this set-up and not for the set-ups used by Wilson and Ford *et al.* The imaginary Γ values resulted when $G_o r < 1 + r$, which implies that $G_o > \frac{1}{r} + 1$. Since $r = I_s(0)/I_p(0)$, then

$$G_o > \frac{I_p(0) + I_s(0)}{I_s(0)} \quad (9)$$

This implies that the law of conservation of energy is somehow being violated. More

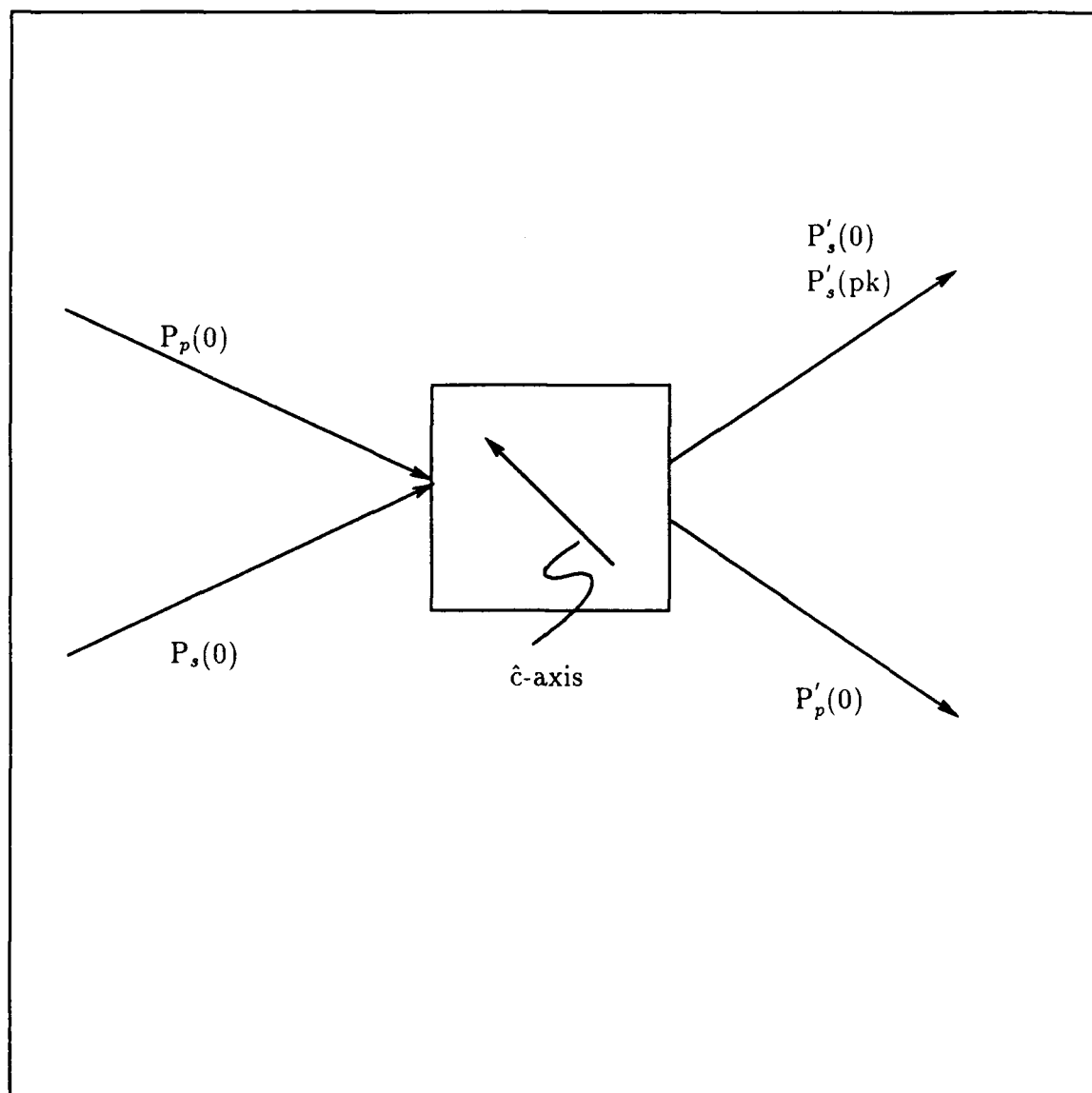


Figure 29. Positions of Power Measurements used to calculate Γ

energy is coming out of the crystal than is being put in. Ford suggested that the portion of the pump beam that does not interact with the signal beam may be reflected back into the crystal off the exit face. This reflected power may cause further amplification of the signal beam. However, this cause of increased gain should have affected the results for Wilson's set-up as well.

Due to difficulties in obtaining realistic Γ values, an input/output gain was determined for each test condition. The behavior of both peak gains, G_{pk} , and steady-state gains, G_{ss} , were investigated. G_{pk} was defined as the ratio of the peak two-wave coupling signal output power, $P_s(pk)$, to the input signal output power, $P_s(0)$. G_{ss} was defined as the ratio of the steady-state two-wave coupling signal output power to $P_s(0)$. Note that no iris was used to measure $P_s(0)$ behind aperture 2, but a 3.0 mm diameter iris was placed over the detector to measure the peak and steady-state output powers.

Input to output gains were investigated for both 45°-cut crystals. Plots of the $\log G_{pk}$ and $\log G_{ss}$ versus the \log of the input beam power yielded surprising results. Figures 30 and 31 are plots of the $\log G_{pk}$ versus the $\log P_s(0)$ for crystals 115-F and 133-E, respectively. The plots imply that a linear relationship exists between $\log G_{pk}$ and $\log P_s(0)$ for a constant pump power over the range of $P_p(0)$ and $P_s(0)$ values tested. Notice that the gains of crystal 133-E are higher than the gains of crystal 115-F for equal input pump and signal beam powers. This was expected because crystal 133-E is slightly longer. The extra length provides a longer interaction region, and therefore, more total gain. It is also interesting to note the slopes of the lines are equal for all pump powers and for both crystals. Figure 32 shows a plot of the $\log G_{ss}$ versus $\log P_s(0)$ for crystal 115-F. The plot suggests that a linear relationship also exists between $\log G_{ss}$ and $\log P_s(0)$ for a constant power over the range of variables tested.

The peak gain was also investigated as a function of the angle β for $P_p(0) = 1.0$ mW, and $P_s(0) = 0.1$ mW. Figure 33 shows G_{pk} versus β for crystal 115-F. The

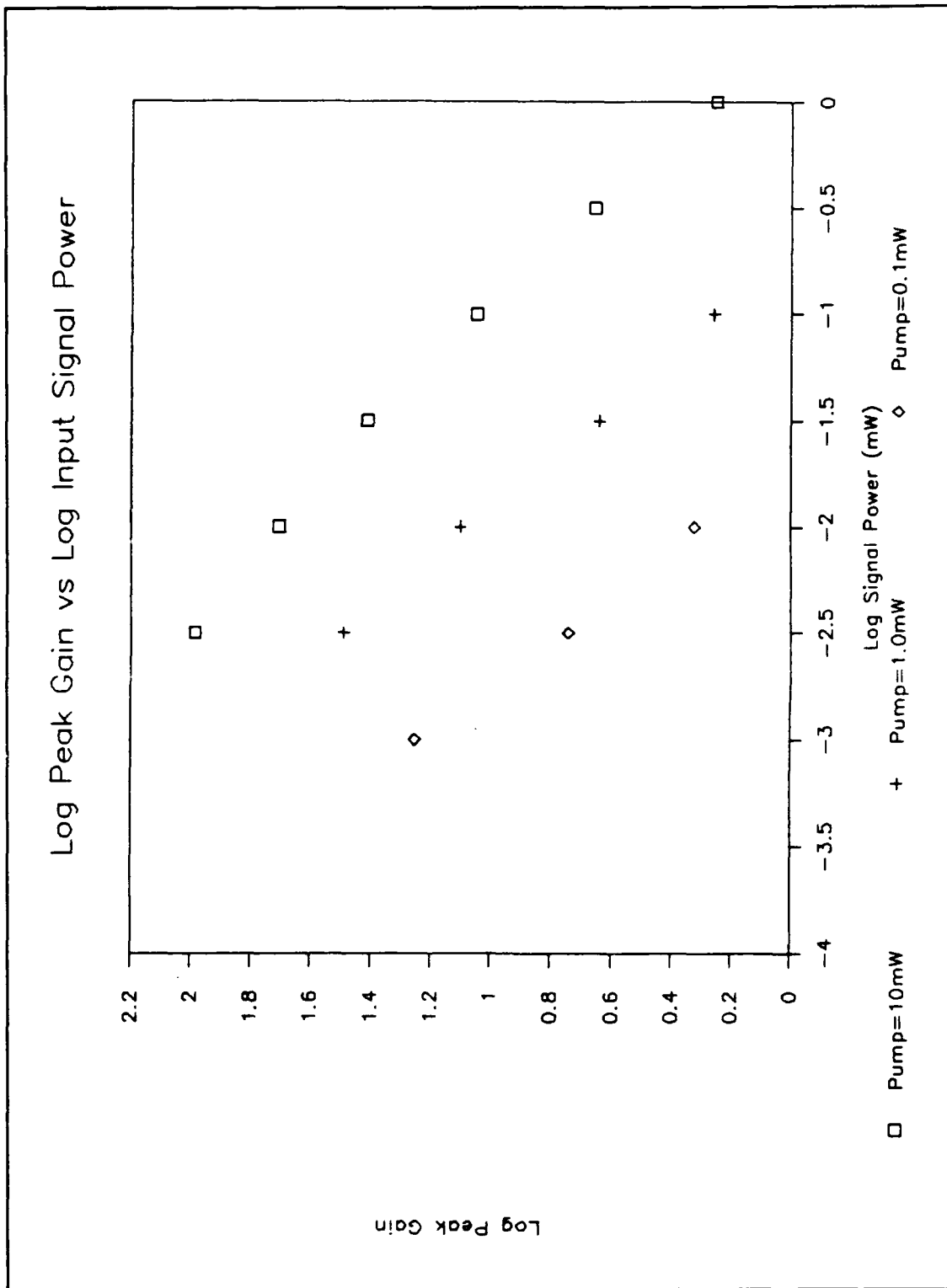


Figure 30. Log G_{pk} versus Log $P_s(0)$ for Crystal #115-F

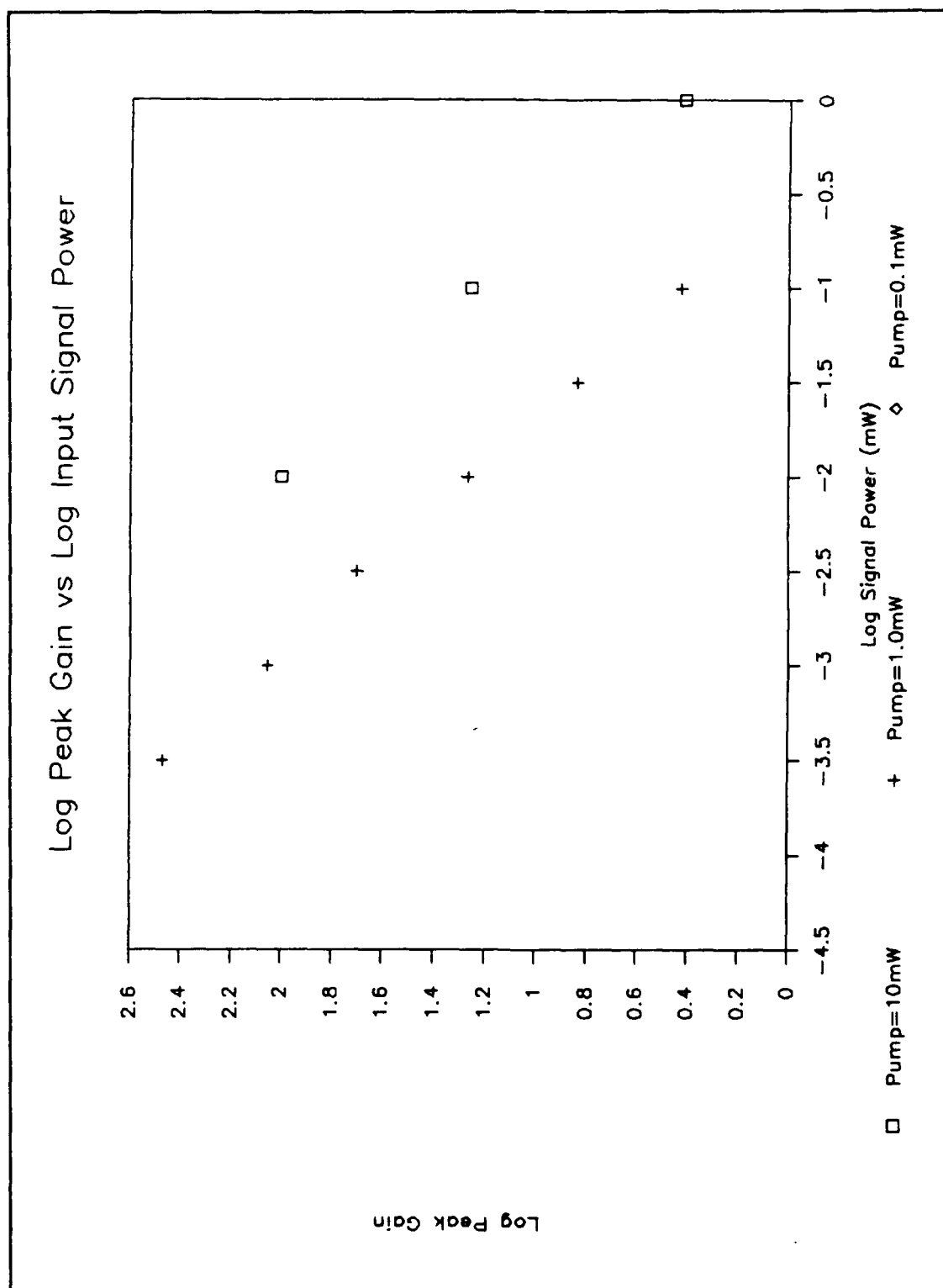


Figure 31. Log G_{pk} versus Log $P_s(0)$ for Crystal #133-E

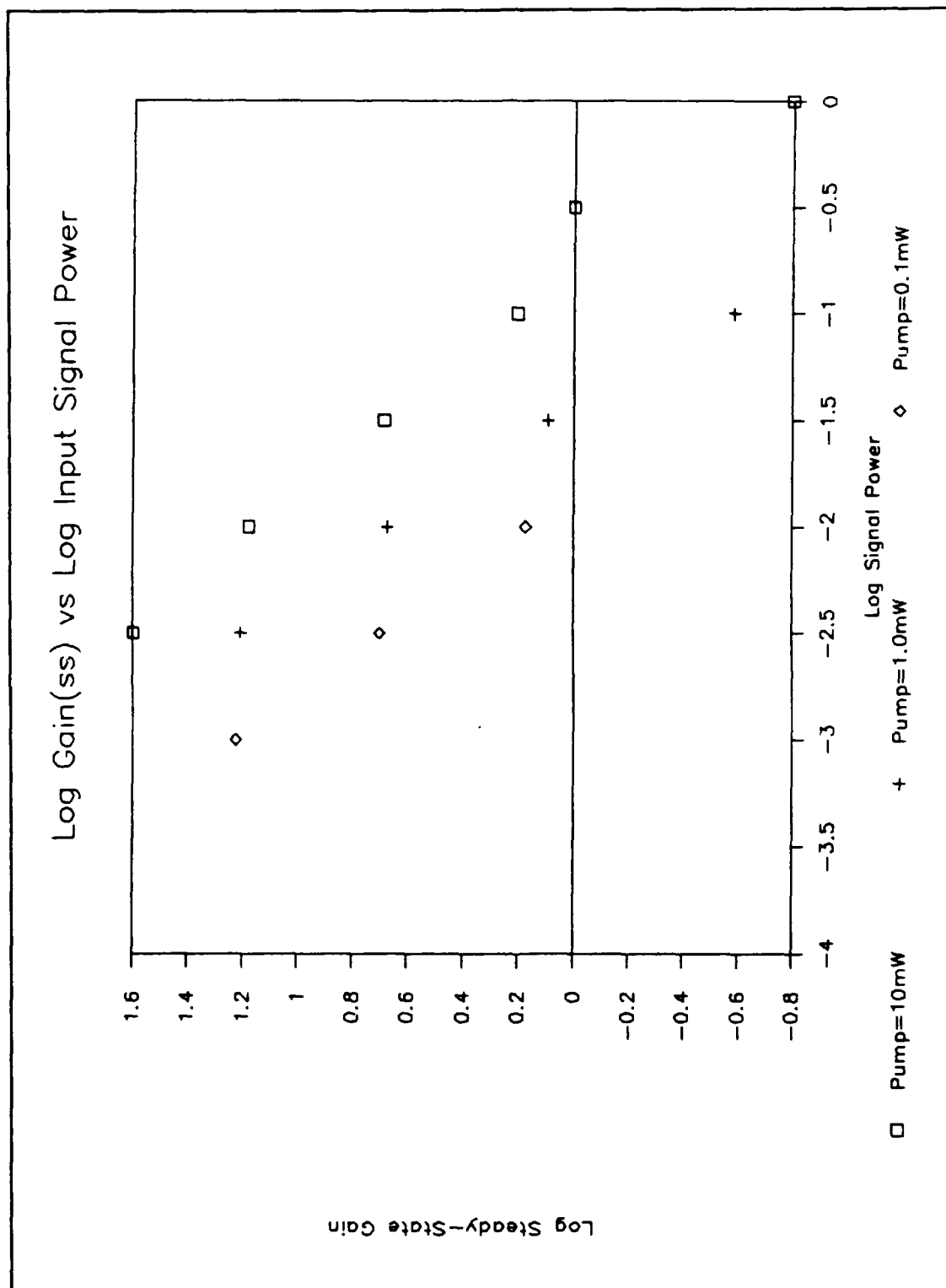


Figure 32. Log G_{ss} versus Log $P_s(0)$ for Crystal #115-F

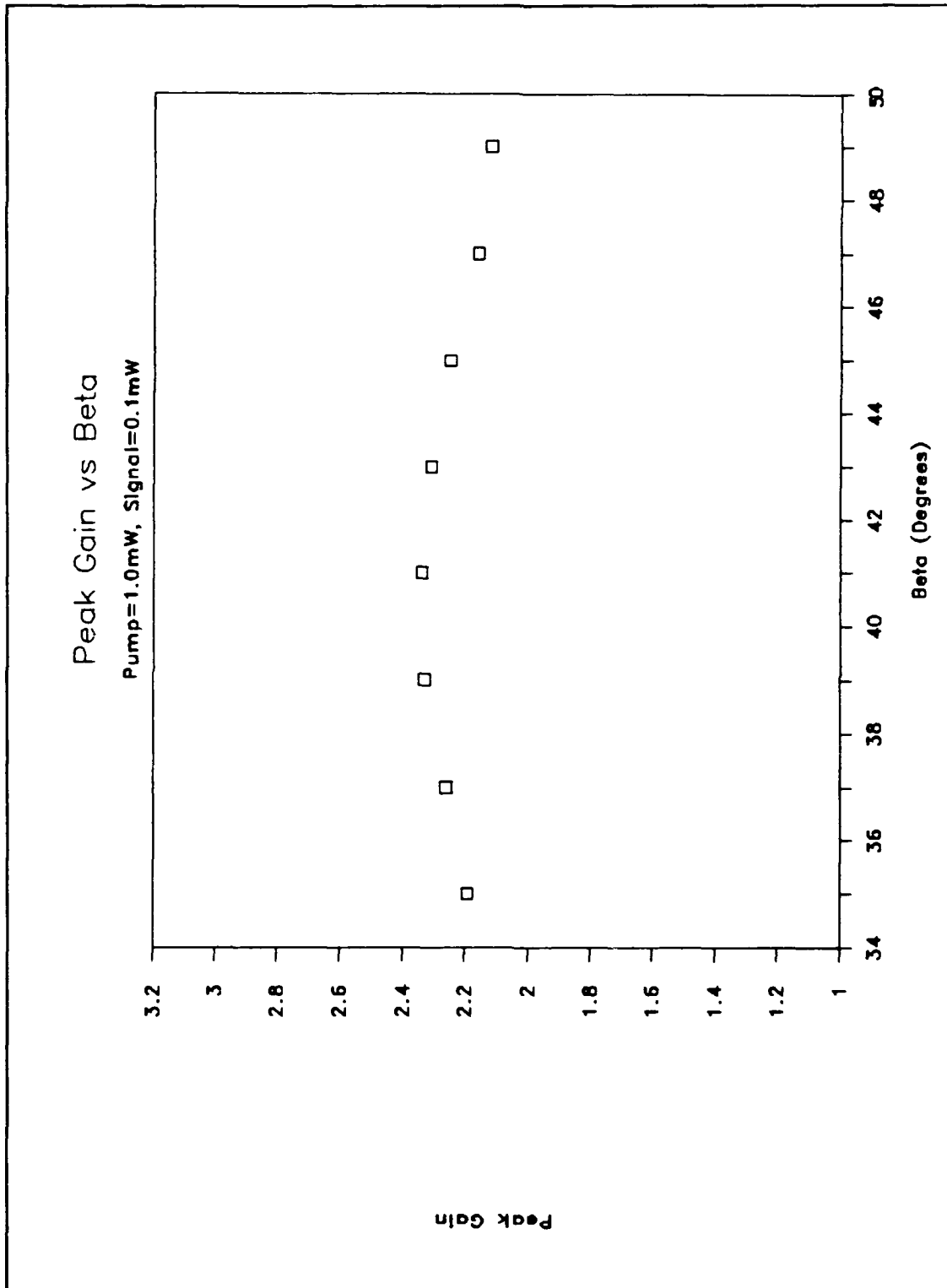


Figure 33. Peak Gain versus β , $P_p(0)=1.0$ mW, $P_s(0)=0.1$ mW

plot shows that the maximum gain occurs near a β of 41 degrees. Recalling that θ was 8 degrees for all test points in Figure 33, the β for maximum gain is comparable to Wilson's results for internal thetas of 2 and 3.5 degrees (25:67).

Two tests were performed with crystal 115-F to investigate the effect of the pump beam fanning on the output signal beam. The first test was a typical two-wave coupling test with $P_p(0) = 1.0$ mW and $P_s(0) = 0.10$ mW. In the second test, the 1.0 mW pump beam was transmitted into the crystal and allowed to fully fan before the 0.10 mW signal beam entered the crystal. Figure 34 shows the two-wave coupling plot for the first test. Figure 35 shows the output signal power versus time for the 'pre-fanned' pump test. The output signal power curves for both tests are remarkably similar. In fact, they are identical except for a slightly higher peak for the first test. The similarity of the two curves suggests that the pump beam fanning is not the cause of the signal beam drop-off observed in two-wave coupling with 45°-cut BaTiO₃ crystals as suggested by Wilson (25:68). Instead, the drop-off appears to be caused only by the beam fanning of the signal beam.

In summary, two-wave coupling with 45°-cut BaTiO₃ was investigated in an attempt to reduce the effects of beam fanning on signal gain. Pump fanning and two-wave coupling pump depletion versus time were compared. Then, transmitted pump and signal power curves for varying input signal powers were presented, and plots of various output signal powers for a constant pump were compared. Pump powers of 1.0 and 10 mW resulted in significant reductions of the signal beam output following an initial rise to a peak value. The signal beam drop-off for a 0.1 mW pump beam was negligible for all signal input powers tested. Steady-state signal beam gains, following rise to the maximum output, were achieved via polarization rotation of the input beams. Next, peak and steady-state gains as a function of input powers and β were presented. A linear relationship between the log of the gain (peak and steady-state) and the log of the input signal power was discovered. Maximum peak gain occurred at a β of 41 degrees. Finally, the results of a pre-fanned pump beam

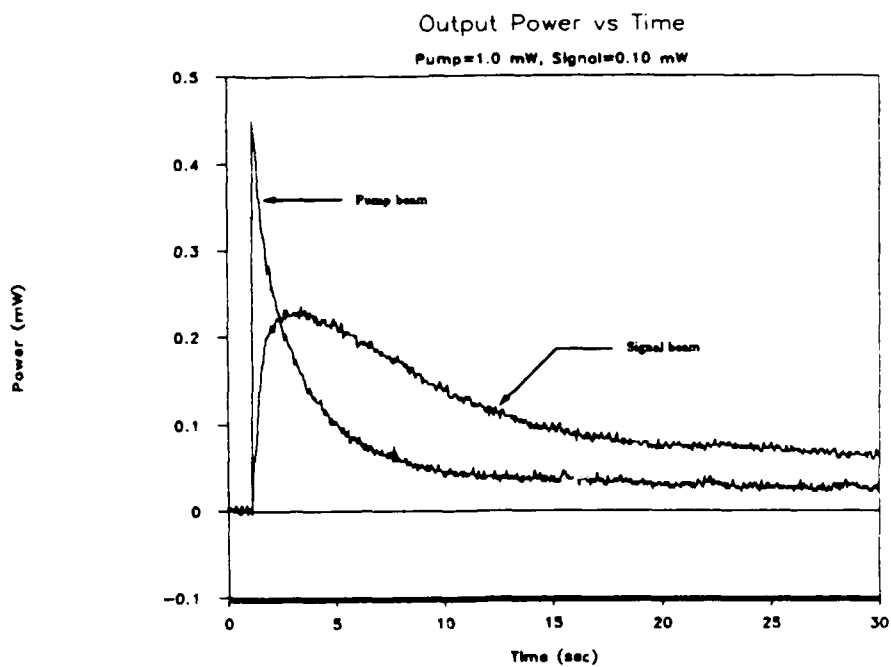


Figure 34. Output Power versus Time, $P_p(0)=1.0$ mW, $P_s(0)=0.1$ mW

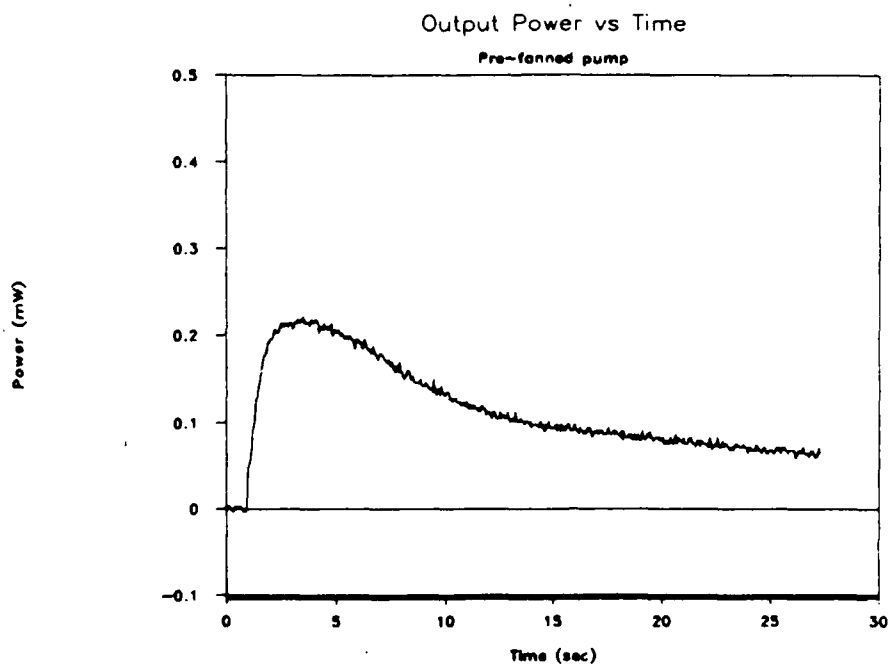


Figure 35. Signal Output Power versus Time for a Pre-fanned Pump Beam

test were compared with a typical two-wave coupling test. The resulting data curves implied that the output signal beam drop-off was due to fanning of the amplified signal beam, instead of the pump beam fanning. In the next chapter, optical image amplification testing will be discussed.

V. Image Amplification Testing

5.1 Introduction

Two-wave coupling and beam fanning tests were required to determine the two-wave coupling geometry for optimum signal gain. Once the geometry to achieve required gain is determined, the image amplification capabilities of the crystal must be characterized prior to use in the resonator. In this chapter, optical image amplification via two-wave coupling with 45°-cut BaTiO₃ is investigated. Background theory and experimental set-ups for amplification of an image and the Fourier transform of an image are described first. Then, test results for both set-ups are discussed.

5.2 Background Theory

Both Fainman *et al.* and Wilson report on the image amplification capabilities of z-cut BaTiO₃ crystals (2:231-233) (25:60-61). However, there are no published reports on such capabilities for 45°-cut crystals. Wilson proposed that a 45°-cut crystal be used for crystal C2 in the Optical Associative Memory architecture shown in Figure 36 (25:27). The basic system operation is as follows. The input image, \tilde{h}^1 , is transmitted through mirror 1 (M1), and then through hologram T1. Transmission through T1 produces the product of \tilde{h}^1 and each of the angle-multiplexed objects stored on T1. Mirror 2 (M2) Fourier transforms each product, and thus, produces a correlation peak for each stored object at the position of a pinhole array (PH). The correlation peaks are attenuated by crystal C1 so that the strongest peak is dominant. This peak is then Fourier transformed by mirror 1. The Fourier transform of the correlation peak is a plane (reference) wave that illuminates the object most like the input stored in hologram T2. Mirror 2 produces the Fourier transform of the object to be recalled at crystal C2. Crystal C2 then amplifies the Fourier transform of the object to provide positive image feedback at T1. A more detailed discussion of the architecture is provided by Wilson (25).

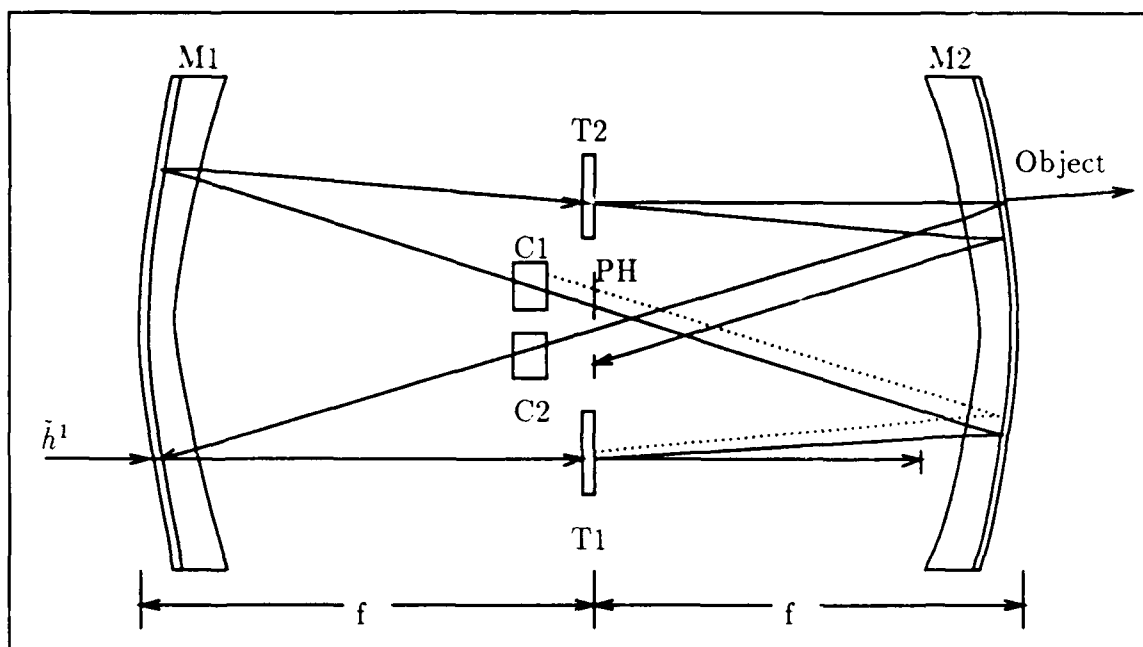


Figure 36. Optical Associative Memory in a Confocal Resonator

Wilson discussed limitations on the stored object's spatial frequency due to the limited size of crystal C2 in the Fourier plane of hologram T2 (25:61). Due to the limitations imposed by this architecture, amplification of both the Fourier transform, and a minified image of a resolution chart were investigated. The experimental set-ups and test procedures used are described in the next section.

5.3 Equipment and Procedure

The experimental set-up used for amplification of the Fourier transform of a resolution target is shown in Figure 37. The same 2 inch diameter collimated output beam used for two-wave coupling testing was used in this set-up. A 50/50 beamsplitter (BS) was used to create the pump and probe beams. A 3.0 mm diameter iris was used to restrict the pump beam diameter. The angle 2θ between the internal pump and signal beams was 16 degrees. Following attenuation by a neutral density filter (NDF) of optical density 2.0, the signal beam illuminated a standard USAF-

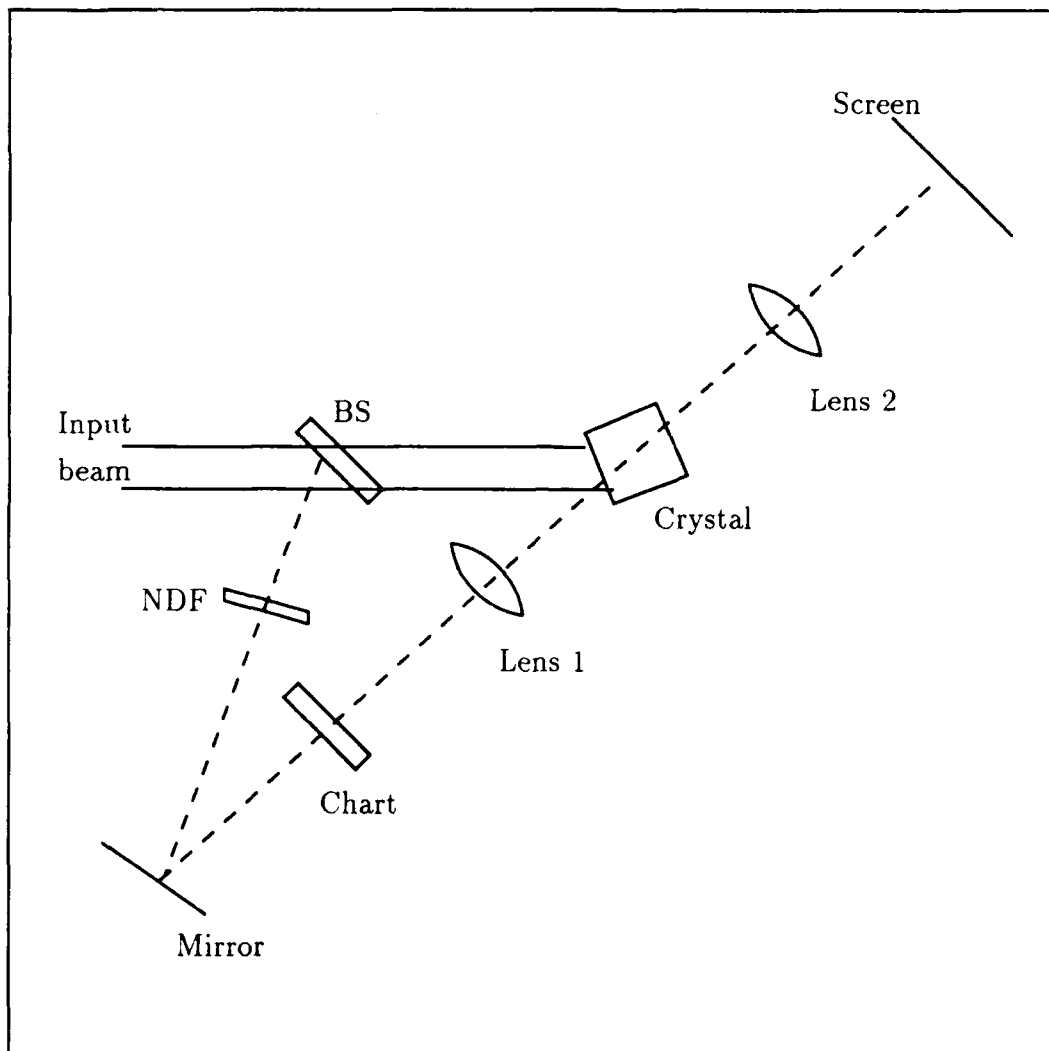


Figure 37. Experimental Set-up for Fourier Transform Amplification

1951 resolution target with an opaque background.

Two lenses, each of focal length 20 cm, were used to observe the image amplification capability of the set-up. Lens 1 was positioned 20 cm from the crystal so that the exact Fourier transform of the target was located at the center of crystal 115-F. Lens 2 was 20 cm behind the crystal center and 20 cm from the imaging screen. This lens was used to create an observable image of the amplified Fourier transform of the resolution target.

Image amplification capabilities of the crystal were tested with the set-up shown in Figure 38. The target, crystal, and pump beams used were the same as described for the previous set-up. Two 12.5 cm focal length lenses were used for imaging. Lens 1 was positioned approximately 60 cm behind the target and approximately 13.5 cm from the crystal. The image distance for an object position of 60 cm and a lens focal length of 12.5 cm is 16 cm via the Gaussian thin lens formula. However, the target image size in the image plane was larger than the crystal dimensions. A shorter length focal lens or a longer object distance could have been used to further reduce the size of the image; however, this was not required. Amplification of the target image's optical field just beyond the back focal length of lens 1 was sufficient to produce observable image amplification.

5.4 Results

Two-wave coupling of the Fourier transform of the resolution target was effective for image amplification. The initial image intensity increased slowly, following initial input of the pump and signal beams. As the original image intensity increased, a secondary image (spatially offset horizontally and vertically from the original image) appeared and increased in intensity. Then, the edges of the bars on the original image increased in intensity relative to the rest of the image to produce an edge enhanced image of the chart. Finally, both images faded in intensity resulting in overlapping, washed out images. Figure 39 resembles a portion of the observed

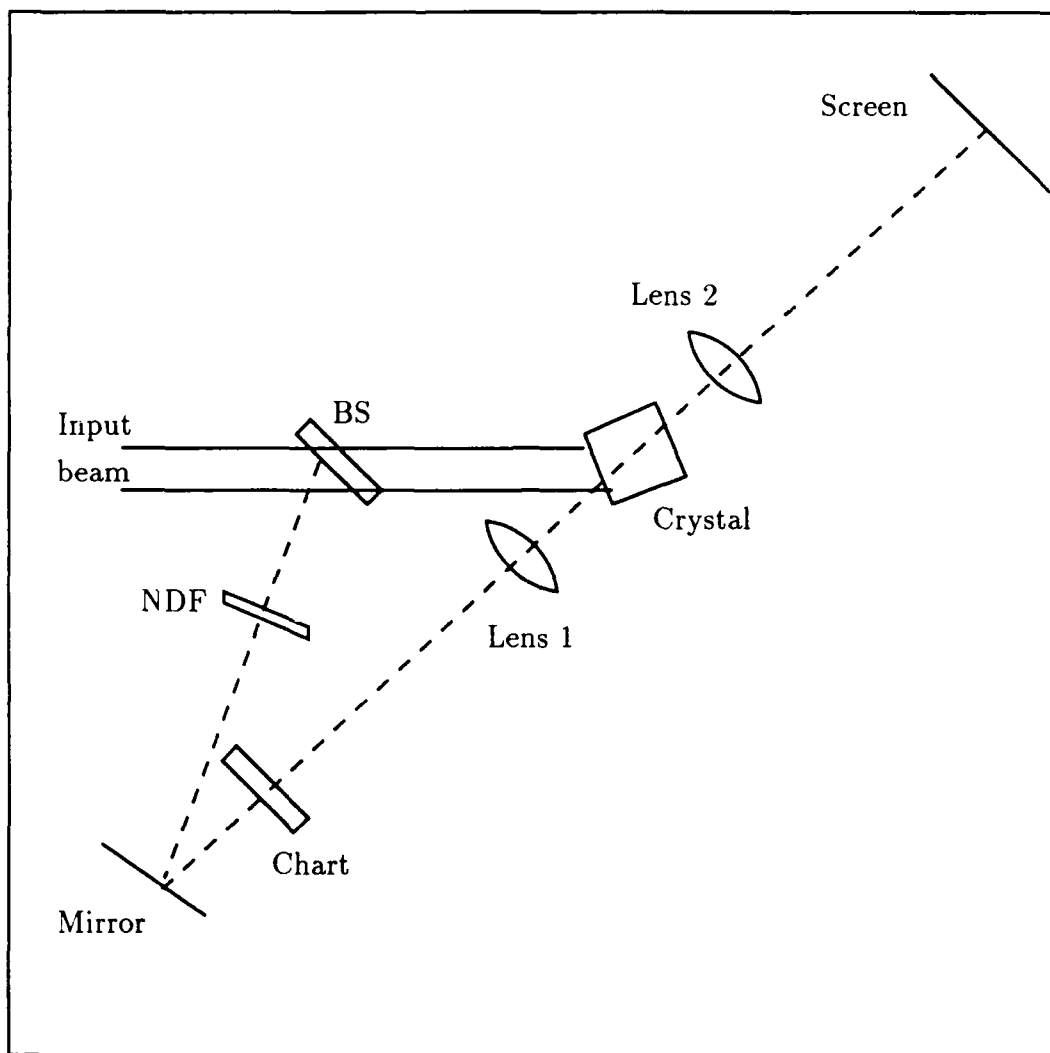


Figure 38. Experimental Set-up for Image Amplification

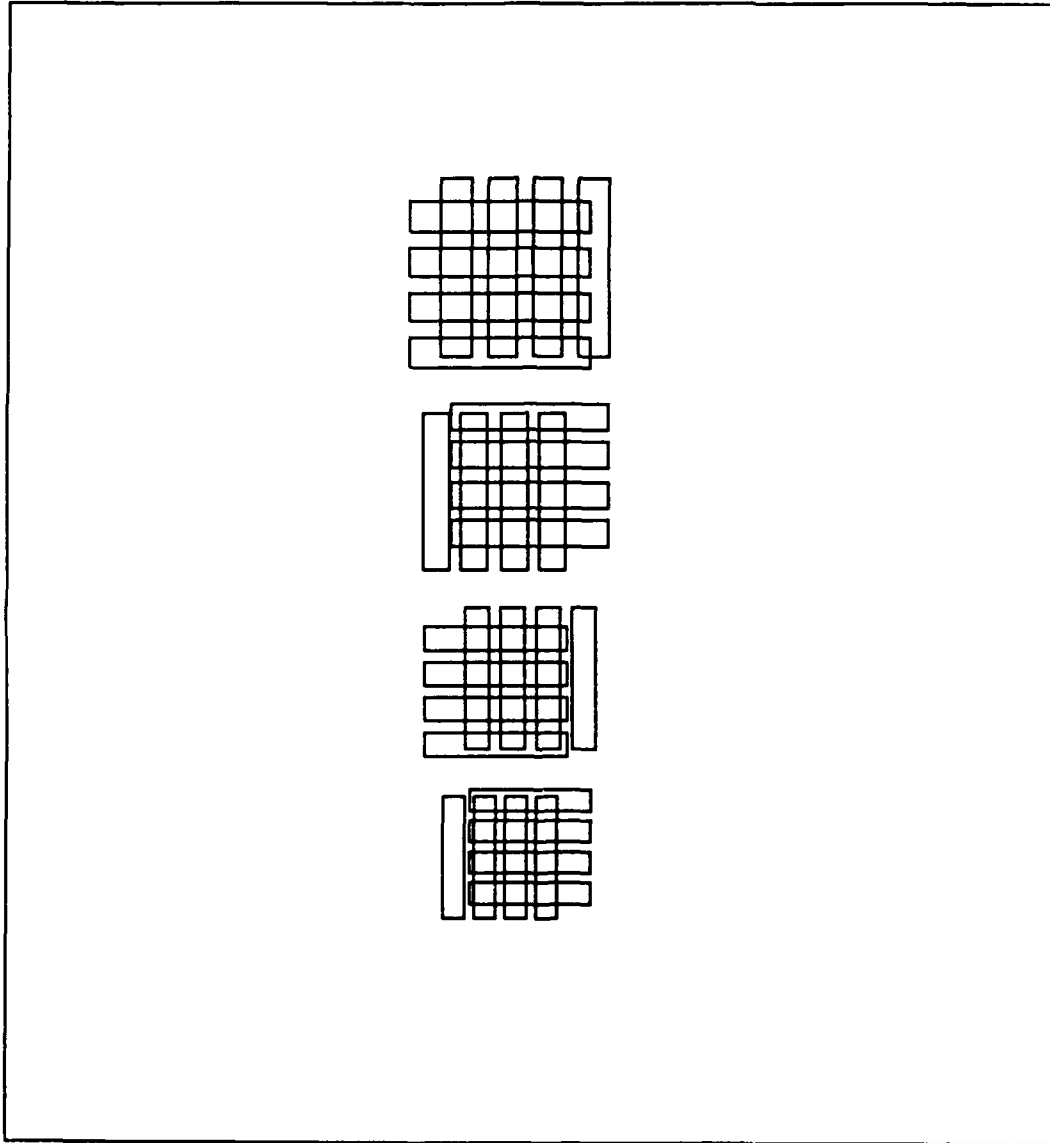


Figure 39. Overlapping Amplified Resolution Chart Image

overlapping pattern.

Higher amplification of the image edges is a result of the lower intensity of the larger spatial frequency components of the image Fourier transform. In the last chapter, input beams of low power were shown to be amplified more than higher power input beams, assuming constant pump beam power. Since the intensity of the larger spatial frequencies is low, the higher spatial frequencies of the image are amplified more than the high intensity, low spatial frequency components. The result is an edge enhanced output image.

The second set of bar patterns appears to be due to the amplification of a double internal reflection of the signal beam as shown in Figure 40. Due to the high index of refraction of BaTiO_3 a portion of the amplified image Fourier transform inside the crystal is reflected off the back face of the crystal toward the entrance face. A portion of the transformed image reaching the entrance face is then reflected back in the same direction as the original image beam. The secondary transformed image is then amplified by the pump beam. The amount of spatial offset between the two observed output images is a function of the angle of incidence between the original signal beam and a normal to the exit face. If the exit or entrance face is tilted vertically with respect to the input signal beam, then horizontal and vertical offsets of the secondary image are possible.

The second test set-up produced similar image amplification results. Illumination of the crystal with the pump and image beams produced an attenuated image of the resolution target at the screen behind lens 2. The intensity of the observable bar patterns increased to a peak value; however, the amplified image was not edge enhanced. Then, as for amplification of the image Fourier transform, a second set of bar patterns (offset, but overlapping the original patterns) appeared and increased in intensity. The final result was a blurred image of two overlapping targets, in which, none of the four bar patterns were distinguishable.

The results from the two set-ups indicate that the image amplification capabil-

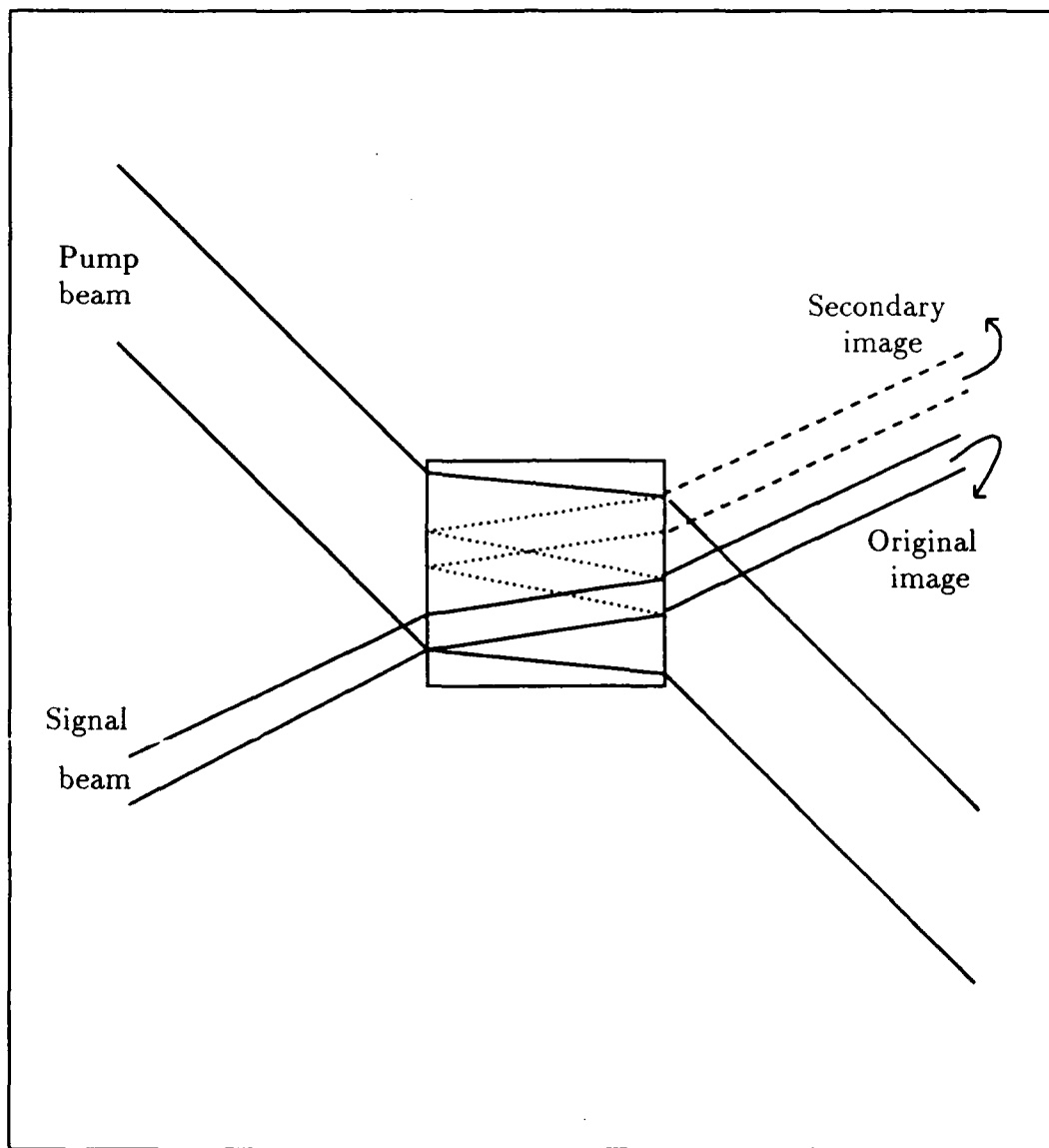


Figure 40. Double Internal Reflection of the Signal Beam

ities of the 45°-cut crystal are limited. Perhaps the best image amplification scheme for crystal C2 would be to use a lens in front of the crystal to produce a minified image, and antireflection coatings at the illumination wavelength (or index matching fluid) to remove the second image. Then use another lens behind the crystal to undo the focusing of the first lens, and thus allow proper feedback at hologram T1. Another consideration when using a 45°-cut crystal for C2, is the drop-off in two-wave coupling gain as time increases. This problem may be alleviated by using sufficiently small pump powers. However, smaller pump powers will of course produce smaller peak gains. The best solution may thus be to rotate the input and output polarizations, as desired, using waveplates.

In summary, two methods for obtaining an amplified optical image with 45°-cut BaTiO₃ have been investigated. Image amplification via two-wave coupling with the Fourier transform of the input image resulted in an edge enhanced image as reported by Wilson for z-cut crystals. Following initial amplification, a second offset/overlapping image was observed prior to complete wash out of both images. Similar results were observed for amplification of a minified image, except that the initial output image was not edge enhanced. Use of a 45°-cut BaTiO₃ crystal as an effective image amplifier in Wilson's proposed architecture will be difficult if at all possible. Conclusions and recommendations based on all testing discussed in this thesis will be presented in the next chapter.

VI. Conclusions and Recommendations

6.1 Conclusions

The major goals of this research were to determine input parameters that minimized beam fanning depletion of a single input beam, find the achievable two-wave coupling gain, and investigate optical image amplification techniques for 45°-cut BaTiO₃. The results of the testing provide an improved understanding of the effects of beam fanning on two-wave coupling gain, and revealed some limitations in the crystal's optical amplification capabilities.

Since Wilson proposed that the loss of two-wave coupling gain in 45°-cut BaTiO₃ was due to beam fanning depletion of the pump beam, methods for reducing fanning of a single 1.5 mm diameter beam were investigated. Input pump beam angles of 40, 20, 0, and -20 degrees from the normal were tested. An input angle of 20 degrees showed the lowest amount of transmitted intensity loss for the angles tested. However, no general conclusions relating input angle and maximum transmitted intensity could be drawn from the test data. An unexpected result, discovered during beam fanning tests, was that the beam fanning of a 1.5 mm diameter input beam was a function of input position on the crystal entrance face (even though the entire beam was contained inside the crystal throughout the transmission path for each position tested).

Two-wave coupling was investigated as a function of input beam powers, polarization, and entrance angles to determine effects of beam fanning on output gain. Beam fanning of the pump beam did not appear to affect the two-wave coupling gain of the signal beam. The reduction in the signal beam output power (following a rise to a peak value) appears to be due only to the fanning of the signal beam itself. Two-wave coupling with an input pump beam power of 0.1 mW and signal beam powers of less than 0.01 mW produced steady-state peak gains (i.e. - there

was little or no beam fanning of the amplified output signal). In addition, a linear relationship between the logarithm of the two-wave coupling peak gain and the logarithm of the input signal power for constant pump powers was discovered. The linear region was demonstrated from a tenth of the input pump power down to input signal powers of 0.001 mW for 1.0 and 0.1 mW pump powers and down to an input power of 0.0033 mW for a pump power of 10 mW. 45° rotations of the input beam polarizations resulted in steady-state maximum gain for an input pump beam power of 1.0 mW and input signal power of 0.1 mW. The steady-state gain was twice that for extraordinary polarized input beams, but less than the peak gain recorded for extraordinary polarization. An internal \hat{c} -axis to grating vector angle, β , of 41 degrees produced the maximum peak gain.

Two methods for achieving image amplification were investigated for use inside Wilson's proposed Optical Associative Memory architecture. Successful image amplification was demonstrated using both methods. Amplification of the Fourier transform of a resolution chart resulted in an edge enhanced output image, but produced two offset/overlapping images and then complete image washout. Similar results were observed for amplification of a minified image, except that the original image was not edge enhanced. Effective optical image amplification with 45°-cut BaTiO₃ in Wilson's architecture will be difficult to achieve.

6.2 Recommendations

The following list contains suggestions for further investigation of optical amplification with 45°-cut BaTiO₃ crystals:

1. Determine the full range of the linear relationship between the logarithm of two-wave coupling gain and the logarithm of input signal power using the same experimental procedures used in Chapter 4. If possible, determine a mathematical expression relating the gain to the input powers;

2. Investigate methods for eliminating the secondary image produced during image amplification (i.e. - index matching fluid or anti- reflection coatings);
3. Compare image amplification capabilities of z-cut and 45°-cut crystals in a confocal resonator with reflective and anti-reflective mirror coatings at 514.5 nm; and,
4. Continue development of the Confocal Resonator Optical Neural Network architecture.

Bibliography

1. Abu-Mostafa, Y. S. and D. Psaltis. "Optical Neural Computers," *Scientific American*: 88-95 (March 1987).
2. Fainman, Y. *et al.* "Optimal Coherent Image Amplification by Two-Wave Coupling in Photorefractive Barium Titanate," *Optical Engineering*, 25: 228-234 (February 1986).
3. Farhat, N. H. *et al.* "Optical Implementation of the Hopfield Method," *Applied Optics*, 24: 1469-1475 (May 1985).
4. Feinberg, Jack. "Asymmetric Self-Defocusing of an Optical Beam from the Photorefractive Effect," *Journal of the Optical Society of America*, 72: 46-51 (January 1982).
5. Feinberg, Jack *et al.* "Photorefractive Effects and Light-Induced Charge Migration in Barium Titanate," *Journal of Applied Physics*, 51: 1297-1305 (March 1980).
6. Fielding, Kenneth H. *et al.* "Position, Scale, and Rotation Invariant Holographic Associative Memory," *Optical Engineering*, 28: 849-853 (August 1989).
7. Ford, Joseph E. *et al.* "Time-Integrating Interferometry using Photorefractive Fanout," *Optics Letters*, 13: 856-858 (October 1988).
8. Ford, Joseph E. *et al.* "Enhanced Photorefractive Performance from 45°-cut BaTiO₃," Article submitted to *Applied Optics*, October 25, 1988.
9. Günter, P. "Holography, Coherent Light Amplification, and Optical Phase Conjugation with Photorefractive Materials," *Physics Reports (Review Section of Physics Letters)*, 93, No. 4: 199-299 (1982).
10. Hecht, Eugene. *Optics*. Reading, Mass.: Addison-Welsey Publishing Company, Inc., 1987.
11. Kogelnik, Herwig. "Coupled Wave Theory for Thick Hologram Gratings," *The Bell System Technical Journal*, 48: 2909-2947 (November 1969).
12. Kukhtarev, N. V. *et al.* "Holographic Storage in Electrooptic Crystals. II. Beam Coupling - Light Amplification," *Ferroelectrics*, 22: 961-964 (1979).
13. Lippmann, Richard P. "An Introduction to Computing with Neural Nets," *IEEE ASSP Magazine*, 4: 4-22 (April 1987).
14. MacDonald, Kenneth R. and Jack Feinberg "Theory of a Self-Pumped Phase Conjugator with Two Coupled Interaction Regions," *Journal of the Optical Society of America*, 73: 548-553 (May 1983).

15. Marciniak, Michael A. *Nonlinear Optical Principles and the Photorefractive Effect Applied to Optical Phase Conjugation*. MS Thesis, AFIT/GEO/ENP/87D-3. School of Engineering, Air Force Institute of Technology (AU), Wright-Patterson AFB, OH, December 1987(AD-A188 856).
16. Marrakchi, A. and J.P. Huignard. "Diffraction Efficiency and Energy Transfer in Two-Wave Mixing Experiments with $\text{Bi}_{12}\text{SiO}_{20}$ Crystals," *Applied Physics*, 24: 131-138 (1981).
17. Moore, Thomas R. and Donald L. Walters. "Observations on Centrosymmetric and Asymmetric Scattering in Barium Titanate," *Journal of the Optical Society of America B*, 5: 1806-1810 (August 1988).
18. Owechko, Y. *et al.* "Holographic Associative Memory with Nonlinearities in the Correlation Domain," *Applied Optics*, 26: 1900-1910 (May 1987).
19. Rupp, R. A. and F. W. Drees. "Light-Induced Scattering in Photorefractive Crystals," *Applied Physics B*, 39: 223-229 (April 1986).
20. Schunemann, P. G. *et al.* "Effects of Feed Material and Annealing Atmosphere on the Properties of Photorefractive Barium Titanate Crystals," *Journal of the Optical Society of America B*, 5: 1702-1710 (August 1988).
21. Staebler, D.L. and J.J. Amodei. "Coupled-Wave Analysis of Holographic Storage in LiNbO_3 ," *Journal of Applied Physics*, 43: 1042-1049 (March 1972).
22. Stoll, H. M. and L-S. Lee. "A Continuous-Time Optical Neural Network," *Proceedings of the IEEE International Conference on Neural Networks*, 2: 373-384 (July 1988).
23. Temple, Doyle A. and Cardinal Warde. "Anisotropic Scattering in Photorefractive Crystals," *Journal of the Optical Society of America B*, 3: 337-341 (February 1986).
24. Valley, George C. "Competition Between Forward-and Backward-Simulated Photorefractive Scattering in BaTiO_3 ," *Journal of the Optical Society of America B*, 4: 14-19 (January 1987).
25. Wilson, Jeffery A. *Optical Information Processing in a Confocal Fabry-Perot Resonator*. MS Thesis, AFIT/GEO/ENG/88D-5. School of Engineering, Air Force Institute of Technology (AU), Wright-Patterson AFB, OH, December 1988. (DTIC number not available at this time).
26. Yariv, Amnon and Pochi Yeh. *Optical Waves in Crystals*. New York: John Wiley and Sons, 1984.

Vita

Kenneth S. Keppler [REDACTED]

He graduated from Rio Americano High School in Sacramento, California in 1977. Following graduation, he attended American River College in Sacramento, California. In 1979, he transferred to the University of California at Los Angeles where he earned the degree of Bachelor of Science in Engineering in June 1983. He then entered the USAF Officer Training School and was commissioned a Second Lieutenant in September 1983. Lt. Keppler was assigned to the 6520th Test Group at Edwards AFB, California where he served as an Avionics Flight Test Engineer. In May 1988, he entered the Electro-Optics Masters Program in the School of Engineering, Air Force Institute of Technology.

[REDACTED]

[REDACTED]

REPORT DOCUMENTATION PAGE

Form Approved
OMB No. 0704-0188

1a. REPORT SECURITY CLASSIFICATION UNCLASSIFIED			1b. RESTRICTIVE MARKINGS		
2a. SECURITY CLASSIFICATION AUTHORITY			3. DISTRIBUTION / AVAILABILITY OF REPORT Approved for public release; distribution unlimited		
2b. DECLASSIFICATION / DOWNGRADING SCHEDULE					
4. PERFORMING ORGANIZATION REPORT NUMBER(S) AFIT/GE0/ENG/89D-5			5. MONITORING ORGANIZATION REPORT NUMBER(S)		
6a. NAME OF PERFORMING ORGANIZATION School of Engineering		6b. OFFICE SYMBOL (If applicable) AFIT/ENG		7a. NAME OF MONITORING ORGANIZATION	
6c. ADDRESS (City, State, and ZIP Code) Air Force Institute of Technology Wright-Patterson AFB OH 45433-6583			7b. ADDRESS (City, State, and ZIP Code)		
8a. NAME OF FUNDING / SPONSORING ORGANIZATION Rome Air Development Center		8b. OFFICE SYMBOL (If applicable) RADC/CA		9. PROCUREMENT INSTRUMENT IDENTIFICATION NUMBER	
8c. ADDRESS (City, State, and ZIP Code) Griffiss AFB, NY 13411			10. SOURCE OF FUNDING NUMBERS		
			PROGRAM ELEMENT NO.	PROJECT NO.	TASK NO.
			WORK UNIT ACCESSION NO.		
11. TITLE (Include Security Classification) OPTICAL AMPLIFICATION IN 45°-cut BaTiO ₃					
12. PERSONAL AUTHOR(S) Kenneth S. Keppler, B.S. Engineering, Capt, USAF					
13a. TYPE OF REPORT MS Thesis		13b. TIME COVERED FROM _____ TO _____		14. DATE OF REPORT (Year, Month, Day) 1989 December	
15. PAGE COUNT 82					
16. SUPPLEMENTARY NOTATION					
17. COSATI CODES			18. SUBJECT TERMS (Continue on reverse if necessary and identify by block number)		
FIELD	GROUP	SUB-GROUP			
09	05		Optical Phenomena Optical Properties		
20	06		Optical Processing Barium Titanate		
19. ABSTRACT (Continue on reverse if necessary and identify by block number)					
<p>Thesis Advisor: Steven K. Rogers, Maj, USAF</p> <p>Associate Professor of Electrical Engineering</p>					
20. DISTRIBUTION / AVAILABILITY OF ABSTRACT <input checked="" type="checkbox"/> UNCLASSIFIED/UNLIMITED <input type="checkbox"/> SAME AS RPT. <input type="checkbox"/> DTIC USERS			21. ABSTRACT SECURITY CLASSIFICATION UNCLASSIFIED		
22a. NAME OF RESPONSIBLE INDIVIDUAL Steven K. Rogers, Maj, USAF			22b. TELEPHONE (Include Area Code) (513) 255-9266		22c. OFFICE SYMBOL AFIT/ENG

UNCLASSIFIED

Abstract

Two-wave coupling in BaTiO₃ has been widely investigated because of the high gains predicted theoretically. Unfortunately, the high gain also amplifies pump and signal light scattered from imperfections inside the crystal. In this report, optical scattering (or beam fanning) and its effects on two-wave coupling gain and image amplification are investigated for 45°-cut BaTiO₃ crystals.

Experimental set-ups for beam fanning, two-wave coupling, and image amplification were designed to investigate signal and image outputs versus time. During beam fanning testing, records of transmitted intensity of a single input beam versus time were obtained for various entrance angles, and input intensities. Pump and signal output powers versus time were recorded for two-wave coupling tests. Input pump beam powers of 10, 1.0, and 0.1 mW were tested at a wavelength of 514.5 nm. Signal input beam powers ranging from 1.0 to .001 mW were used. In image amplification tests, the Fourier transform and a minified image of a resolution chart were amplified via two-wave coupling.

Data from beam fanning and two-wave coupling tests implied that the beam fanning of the pump beam has negligible effect on the two-wave coupling gain of the output signal. Following rise to a peak value, the output signal beam power decreased due to fanning of the amplified signal beam for input pump powers of 10 and 1.0 mW. Little or no drop-off was observed for the 0.1 mW input pump power. A linear relationship between the logarithm of the gain (peak and steady-state) and the logarithm of the input signal power was discovered over the entire range of the input pump and signal powers tested. Amplification of the resolution chart's Fourier transform resulted in an edge enhanced image. Secondary images were observed for both image amplification set-ups.

UNCLASSIFIED